university of groningen / faculty of science and engineering / zernike institute for advanced materials

Microwave driving of transition metal defect spins coupled to nuclear spins in SiC

Author: Irina Ion

Supervisor: prof. dr. ir. Caspar van der Wal
Daily supervisor: MSc Carmem Maia Gilardoni

Second examiner: prof. dr. Richard Hildner

Master Thesis for the Program:

MSc Physics - Advanced Materials
Zernike Institute for Advanced Materials
Faculty of Science and Engineering
University of Groningen
Groningen, the Netherlands

September 2019 - July 2020

Abstract

External control over fundamental quantum mechanical phenomena paves the way to novel applications in areas of communication and computation. Quantum cryptography, quantum memories, quantum networks and quantum computers rely on the ability to store, process and communicate quantum information. Color centers in silicon carbide (SiC) are a promising platform for such applications, as they provide localized electronic spin states that can function as qubits. These defects are bright optical emitters with long spin coherence time, and enable interfacing with photons in the (near-) telecom range. At the same time, their integration into a host material like SiC, which is industrially-mature, allows relatively easy fabrication and integrability into more complex devices. In this work, we focus on the highly anisotropic system of molybdenum and vanadium defects in SiC. Although recent experimental and theoretical investigations have unraveled many of their spin properties, they have also raised significant questions: theoretical investigations suggest that driving spin resonances in the ground state of these defects should be forbidden by the symmetry of the defect. Nonetheless, recent experimental work on V defects in SiC show clear microwave driving of the defect spins. Here, we use a first-principles approach to investigate whether this apparent discrepancy can be resolved by considering the interactions between electronic and nuclear spins via the hyperfine interaction.

Furthermore, we present our results using a visualization tool in the form of color maps, which mitigates challenges in dealing with high-dimensional Hilbert spaces. Given the model used and the interactions considered, this visualization tool allows us to conclude that microwave driving is only enabled by the hyperfine interaction for a specific set of electronic spin states.

Contents

1 Introduction

Quantum information technologies aim at using fundamental quantum phenomena in systems specifically designed for quantum computation or quantum communication. The ability to store, process and communicate quantum information would not only allow for fundamentally secure communication, but also enable tackling computational problems currently unachievable [1]. For these reasons, quantum platforms that can be coupled over long distances have been widely explored in the past decades [2]. Although various platforms have been studied for possible applications in this context, defects in solid-state systems are particularly interesting as they could be easily integrated into devices [3], [4], [5]. Solid-state systems with few- or single-quantum states which can be addressed via radiation of characteristic wavelengths could present a further advantage: being able to exploit existing telecommunication infrastructure for transmitting information over long distances [6]. Since minimum losses occur in the near- and infrared region, an obvious research direction is looking into systems that allow read-out at (or a subsequent efficient conversion to [7], [8]) such wavelengths.

Certain defects in wide-bandgap semiconductors offer well isolated and long-lived quantum states that can be addressed and read-out optically [9]. Silicon carbide (SiC), a wide bandgap semiconductor, is an industrially mature material that can host a number of interesting defects, so-called color centers. These defects can be intrinsic, in the form of single or multiple vacancies (a missing intrinsic atom) or extrinsic, containing various types of atoms introduced in the lattice in a controlled way. Particular transition metal atoms embedded in the crystal act as extrinsic color centers in silicon carbide. Defects containing molybdenum (Mo) or vanadium (V), for example, have shown long spin lifetimes and couple well to radiation in the (near-) telecom bands.

In this work, we theoretically investigate defects containing Mo impurities in SiC, focusing on characterization of their quantum spin states. Understanding how these states appear and how to manipulate the spin is not only vital for potential applications, but also interesting for a fundamental understanding of the quantum mechanical processes at play. Previous theoretical work has shown that the properties of these defect spins are largely determined by the valence electrons in the transition metal impurity. Thus, we expect the results of this study to be relevant for other transition metal defects, with analogous valence number and crystalline environments, such as V defects. Although recent experimental and theoretical investigations have unraveled many of their spin properties, they have also raised significant questions: theoretical investigations suggest that driving spin resonances in the ground state of these defects should be forbidden by the symmetry of the defect. Nonetheless, recent experimental work on V defects in SiC show clear microwave driving of the defect spins. Here, we investigate whether this apparent discrepancy can be resolved by considering the interactions between electronic and nuclear spins via the hyperfine interaction.

In what follows, Chapter 2 provides the background necessary for our investigation, particularly

on the concepts of color center and spin control, the 6H-SiC polytype as defect host, and transition metal defects. Experimental results for Mo and V in SiC are included there as well. Chapter 3 includes a detailed discussion of the interactions that play a large role in the characterization of these defects in the context of qubit applications. These interactions are quantified in Chapter 4, where the nuclear spin is also included in the description. Here, we present a tool for visualizing high-dimensional matrices which will be used when later discussing the hyperfine interaction in Chapter 5. Finally, Chapter 6 presents the conclusions of this investigation, and possible further steps.

2 Color centers in silicon carbide

2.1 Color centers

Color centers are optically active defects in a wide-bandgap semiconductor host. Contrary to what their name suggests, they can not only exhibit luminescence in the visible region, but in the infrared as well. They change the optical properties of the otherwise defect-free host semiconductor by adding localized energy states within its wide bandgap. These effectively locally trapped electronic spin states can function as qubits in devices, provided their manipulation and interfacing with information-carrying photons can be done reliably. The negatively-charged nitrogen vacancy (NV^-) center in diamond has been extensively investigated for applications in quantum information processing and quantum sensing [10], [11]. This defect has shown long spin lifetimes even at room temperature, and can have applicability in quantum memory devices. Furthermore, the NV^- center in diamond can act as a single photon source which is important for quantum cryptography. Lastly, their use as qubits in general is viable, due to proven spin control and read out with high fidelity .

2.2 Spin control via microwave driving

The qubits of information in such a solid state system are encoded in the few-level quantum system created by the lowest, isolated color center electronic spin states. Manipulation of information presumes the ability to control the electronic spin. The spin can be in one of two states, which we denote $|0\rangle$ and $|1\rangle$, or a superposition of the two. Often, spin control is done via microwave driving, where an oscillating magnetic field couples to the electronic spin and provides the energy required for a transition between states $|0\rangle$ and $|1\rangle$. This process is known as electron spin resonance and is described by the phenomenological Hamiltonian:

$$H = -\frac{\mu_B g_z}{\hbar} B_0 \sigma_z - \frac{\mu_B g_{x,y}}{\hbar} B_1 cos(\omega t) \sigma_{x,y} \tag{1}$$

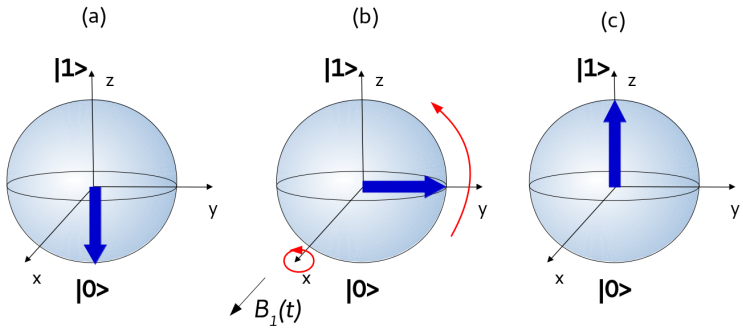

Figure 1: Illustration of a two-level spin system in a Bloch sphere. The z-axis is the quantization axis determined by an applied magnetic field in the $\hat{z}$ drection or by the system's symmetry. a) Initially, the spin is found in the $|0\rangle$ state with probability 1. b) Upon applying a time-varying magnetic field in a perpendicular direction ($\vec{B}_1(t) \parallel \hat{x}$), here the $\hat{x}$ direction, the spin will start to precess about the x-axis. The spin is now in a superposition of states $|0\rangle$ and $|1\rangle$. c) After a specific time, it will end up in the $|1\rangle$ state with probability 1.

where μ_B is the Bohr magneton; B_0 is a static component of an externally applied magnetic field; B_1 is the dynamic component of the oscillating magnetic field with frequency ω; $\sigma_{x,y,z}$ represents either of the three Pauli matrices for a two-level system in a cartesian coordinate system defined by $\hat{x}, \hat{y}, \hat{z}$; and $g_{x,y,z}$ are the diagonal components of the g-factor tensor, which gives the coupling between a spin state and an applied magnetic field. The spin quantization axis, $\hat{z}$, is defined here by the direction of $\vec{B}_0$.

Fig. 1 illustrates a two-level spin system with a spin-down ($\equiv |0\rangle$) and a spin-up ($\equiv |1\rangle$) state, defined with respect to the quantization axis defined by the direction of $\vec{B}_0$. Classically, an oscillating magnetic field perpendicular to the quantization axis allows the spin to precess around the axis defined by B_1. Thus, the electronic spin state is modified deterministically by the presence of the field B_1. Control of the field direction and strength, as well as microwave driving time provide spin control. Previous experimental investigations performed by T. Bosma et al. show that for Mo in SiC, this proves problematic [13]. Their experimental work has shown that the ground state spins in these defects are insensitive to a static magnetic field applied perpendicularly to the symmetry axis of the defect. This translates into $g_{x,y} = 0$ (from eq. 1). Looking at the ESR Hamiltonian in eq. 1, this would mean that electronic spin resonance is not possible.

2.3 Silicon carbide

Silicon carbide is a wide-bandgap semiconductor that hosts a myriad of optically active defects in the (near-) telecom range. Research focus sparked by the potential shown by NV^- centers in diamond has shifted towards SiC, a material that allows more efficient fabrication and integrability into devices [14]. SiC has many polytypes, each with a different bandgap, and embedded color centers can occupy several sites. These features give room for a variety of potential device designs with applicability in quantum computation, information, and sensing [15] - [17]. Furthermore, SiC

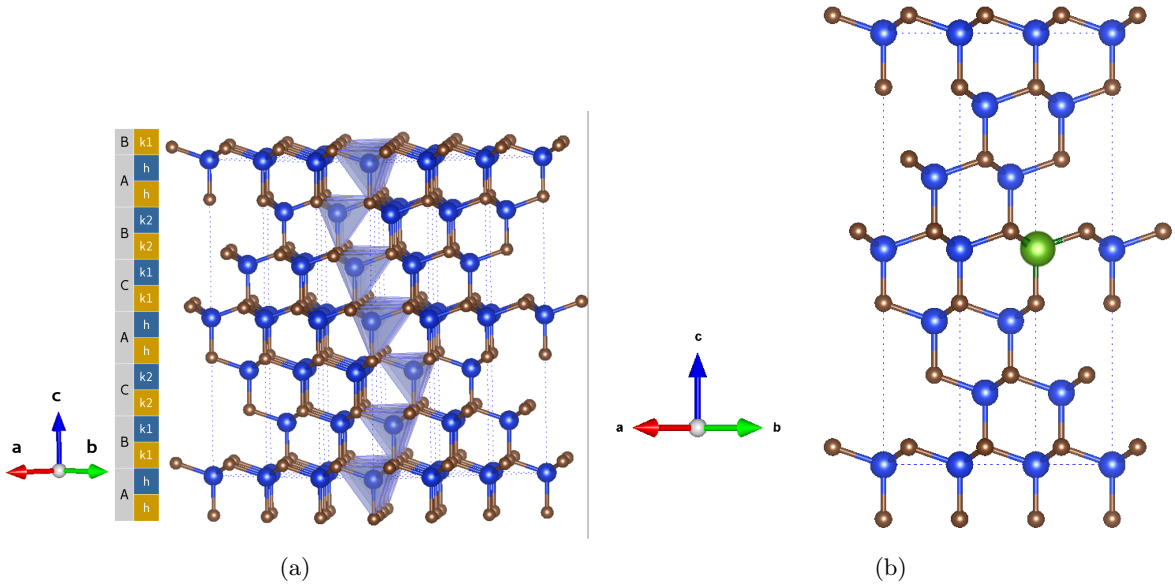

(a) (b)

Figure 2: 2a: Crystal structure of 6H-SiC, with layers forming a unit cell ordered as ABCACB, in a hexagonal axis system $(\hat{a}, \hat{b}, \hat{c})$. The so-called quasi-hexagonal symmetry and quasi-cubic symmetry sites are labeled h, and $k_{1,2}$, respectively. The repeating stacks of tetrahedra which form SiC are highlighted as four carbon atoms (brown) surrounding a silicon atom (blue). 2b: Molybdenum atom (green) substituting silicon at a hexagonal site in 6H-SiC. Mo has as nearest neighbors four carbon atoms in a tetrahedral configuration. The spatial arrangement of its next-nearest neighbors gives rise to a trigonal field. At this site in a p-type material, Mo is in the electronic configuration $Mo^{5+}(4d^1)$, i.e. it has a single valence electron in relatively isolated d-orbitals. These crystal structures were created using VESTA software.

provides an essentially nuclear spin-free environment: the natural abundances of non-zero nuclear spin Si and C isotopes are approximately 4% and 1%, respectively. The mixed lattice further reduces the influence of the nuclear spins bath on localized impurities [18]. This is a good starting point for a well-isolated spin quantum system, and it can be further improved through isotopic purification.

Two of the most studied polytypes of SiC are 4H-SiC and 6H-SiC, which have mixed cubic and hexagonal stacking of layers. Their unit cell consists of 4 and 6 stacks, respectively, of Si-C bilayers, with Si and C atoms in tetrahedral coordination. Fig. 2a shows the crystalline structure of 6H-SiC, with stacking order ABCACB. Each Si or C atom can be labeled by the symmetry of its environment, as h, k_1, k_2, where h refers to quasi-hexagonal symmetry, and the two ks denote quasi-cubic symmetry. The symmetries of these sites can be understood from the configurations of next-nearest neighbors. For instance, the next-nearest neighbors of a Si atom are 6 in-plane Si atoms, and 3 Si atoms in each of the above and below layers viewed along the crystalline c-axis. If this Si atom is at an h-site, the next-nearest neighbors in the above and below layers have an identical configuration along the c-axis. For a $k_{1,2}$ site, these same neighbors are rotated away from each other about the c-axis.

The same lattice site denomination from Fig. 2a can be used for labeling the site occupied by a color center embedded in SiC. Due to varying local symmetries, the SiC polytype and the site

occupied by the color center will influence the characteristics of the defect states.

2.4 Molybdenum defect

The Mo and V defects have been extensively investigated in recent literature. They are optically active, with bright zero-phonon lines (ZPL) at 1121 nm, and around 1300 nm, respectively ([13],[19]). Spectroscopy of the ground and optically excited states' spin structure shows that they behave as an effective spin-1/2 system. That is, both the ground and the optically excited states are doublets whose degeneracies are lifted when a static magnetic field is applied. Furthermore, the Zeeman energies associated with these doublets increase linearly with increasing magnetic fields. Curiously, the magnitude of the Zeeman splitting depends on the direction of the magnetic field with respect to the crystal c-axis. When the field is applied parallel to the c-axis, the observed splitting is relatively large, and it allows extracting coupling parameters $g_{\parallel}^{|g\rangle} = 1.61$, $g_{\parallel}^{|e\rangle} = 1.20$, for the ground and optically excited state of the Mo defect, respectively. For a field in the basal plane, perpendicular to the c-axis, no Zeeman splitting is observed in the ground state of the Mo defect, such that $g_{\perp}^{|g\rangle} = 0$. A small splitting corresponding to $g_{\perp}^{|e\rangle} = 0.11$ is seen in the optically excited state of the same defect. Theoretical work based on analysis of the atomic orbitals of the Mo ion and the symmetries of the defect have largely unraveled the origin of these effects [13]. It was shown that Mo (Z = 42) atoms embedded in 6H-SiC most likely occupy a hexagonal (h) Si substitutional site, as depicted in Fig. 2b.

Here, Mo forms covalent bonds to the four surrounding carbon atoms, and donates one electron to the p-type SiC lattice, thus retaining the electronic configuration $Mo^{5+} = [Kr]4d^1$. In this lattice site, Mo is subject to both tetrahedral and trigonal crystal fields that act on the valence electron 4d-orbitals. Furthermore, since Mo is a heavy atom, spin-orbit coupling (SOC) is expected to play a significant role. A combination of the rotational symmetry of the defect and SOC locks the electronic spin along the rotational symmetry axis, leading to the strong anisotropy observed in the Zeeman splitting.

According to this alone, and considering eq. 1, electron spin resonance for Mo in 6H-SiC is not possible. Subsequently, due to the analogous electronic structure, the same should apply to V. However, Wolfowicz et al. ([12]) showed very recently that this is not the case for V^{4+} in 4H-SiC. They were able to drive spin resonance between the defect's two ground state spins using an oscillating field B_1 along the crystalline c-axis. They assign this effect to interactions between electronic and nuclear spins of the V defect. Similarly to the Mo defect in 6H-SiC, the V defect has a single valence electron in its d-orbitals ($3d^1$), and a high nuclear spin. Moreover, their experiments show that spin resonance was only weakly seen for B_1 in the basal plane, which suggests that the Mo and V defects in SiC are described by similar symmetry.

Previous experimental and theoretical investigations on Mo defects have, however, overlooked the role of the nuclear spin degree of freedom in their interpretation of results. The samples used

in experiments by T. Bosma et al. [13] are not isotopically purified, such that about 25% of the Mo atoms have nuclear spin $i = \frac{5}{2}$, while the remaining have $i = 0$. Similarly, V atoms have nuclear spin $i = \frac{7}{2}$ in 99.8% proportion (the rest of isotopes have $i = 6$). It is therefore sensible that, in order to understand the full set of interactions allowed for the defect, we must consider the effects of those nuclear spins via the hyperfine interaction.

3 Characterization of the Mo defect in the SiC crystal

In this chapter, we further present the qualitative analyses used to explain the anisotropic Zeeman splitting of spin states of a Mo defect in 6H-SiC. We present a model including the effects of the crystal fields and spin-orbit coupling on the Hamiltonian associated with the defect, based on work done by F. Hendriks [20]. Furthermore, we are interested in characterizing the defect spins' interaction with an external magnetic field. To this end, we present an effective spin Hamiltonian for the Zeeman interaction that allows extracting a phenomenological g-factor, and subsequently compare this to the real Hamiltonian of the interaction.

3.1 Departure from the free Mo ion

In order to understand the electronic structure of Mo in 6H-SiC, we start with those interactions that we expect are strongest in perturbing the configuration of a free Mo^{5+} ion. The single valence electron occupies the ion's 4d-orbitals which, in a free environment, are five-fold orbitally degenerate. This degeneracy becomes ten-fold if we include the electronic spin. The 4d-orbitals are described by orbital angular momentum quantum number $l = 2$, with quantization given by the quantum number $m_l = \{-2, -1, ..., 2\}$. The spherical harmonics $Y_2^{m_l}(\theta, \phi) \equiv \langle \theta\, \phi | l\, m_l \rangle$ (in Dirac notation) are functions that represent the electronic density in the space described by a set of angles (θ, ϕ). In a spherically symmetric environment, these functions are eigenfunctions of the operator $\mathbf{L}^2$, and are thus degenerate. Distortions introduced by the cubic and trigonal crystal fields lower the spherical symmetry of the free ion, breaking the five-fold degeneracy.

In addition, in describing the single valence electron states of the Mo ion in 6H-SiC, we assume the Mo-C bonding electrons do not contribute to the total spin angular momentum of the defect. In the ground state of the defect, all bonding electronic spins are paired. Thus, the spin carried by the single valence electron, with quantum number $s = \frac{1}{2}$, gives the total spin angular momentum for our system.

Thus, in order to describe the states that the defect's single valence electron spin can occupy, we use the decoupled basis of spin-orbitals, $|l\, m_l; s\, m_s\rangle$, with $l = 2$ for d-orbitals, $m_l = \{-2, -1, ..., 2\}$, $s = \frac{1}{2}$, and $m_s = \{-\frac{1}{2}, \frac{1}{2}\}$. As concerns notation, we write $|l\, m_l; s\, m_s\rangle = |m_l\, m_s\rangle$ to describe a ten-dimensional space spanned by this basis, since l , s do not change.

3.2 Crystal fields

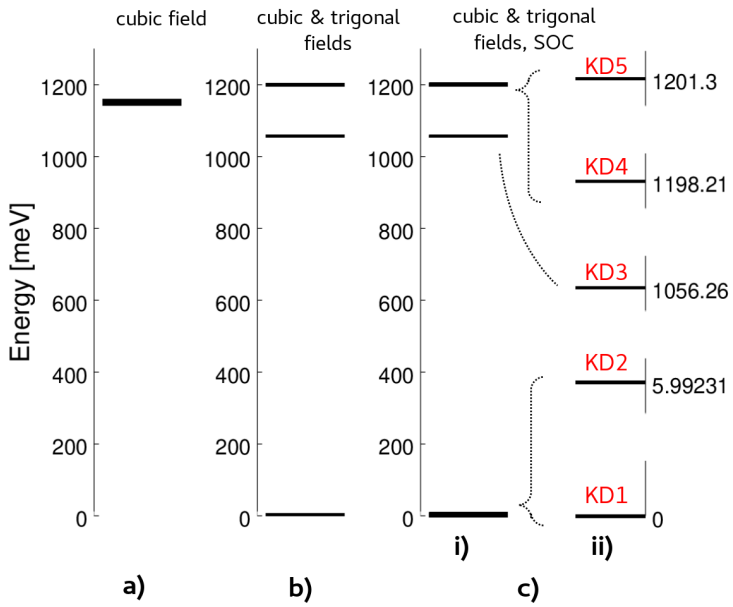

Figure 3: Energy diagrams for Mo 4d-orbitals at a h Si substitutional site in 6H-SiC: a) in the presence of a weak cubic crystal field due to the tetrahedral configuration of nearest neighbors. This field splits the original 5 orbitals states into an orbital doublet and an orbital triplet. b) A stronger, trigonal crystal field is added, which leads to further splitting of the orbital triplet into an orbital doublet and an orbital singlet, and mixes the eigenstates of the cubic field. c) - i) Spin-orbit coupling (SOC) further splits the orbital doublets and mixes them. The electronic configuration is then composed of 5 Kramers doublets, shown magnified in ii). The KDs are labeled by increasing energy. The energies shown here are eigenvalues of Hamiltonian $H_0 = H_{Td} + H_{C3v} + H_{soc}$, presented below, for the parameters given in Table 4.

The effects of the cubic and trigonal crystal fields are shown in Fig. 3 a), and b), respectively. The splitting observed due to the crystal fields can be understood by considering that the Coulomb interaction between the unpaired electron and the bonding electrons is highest at the points in space where their wave functions overlap. Thus, compared to the free ion, where all directions are equivalent, an energy difference appears between the unpaired electron states that involve various degrees of overlap with the neighboring atoms. Based on the symmetry of the crystal fields, F. Hendriks describes in [20] the crystal field Hamiltonian associated with the defect. The Hamiltonians H_{Td} and H_{C3v} related to the cubic and trigonal crystal fields are diagonal in the bases of ordered cubic harmonics $S_1 = \{d_{z'^2}, d_{x'z'}, d_{y'z'}, d_{x'y'}, d_{x'^2-y'^2}\}$ and $S_2 = \{d_{z^2}, d_{xz}, d_{yz}, d_{xy}, d_{x^2-y^2}\}$, respectively. The two sets of basis states transform into one another under a rotation. In the primed basis, $H_{Td} = diag(E_{Od}, E_{Ot}, E_{Ot}, E_{Ot}, E_{Od})$, and $H_{C3v} = diag(E_{C0}, E_{C1}, E_{C1}, E_{C2}, E_{C2})$ in the unprimed basis.

These Hamiltonians are equivalent to the observation that a cubic field with symmetry T_d causes the five d-orbitals to split into a triplet (Ot) and a doublet (Od) state, due to the spatial inequivalence created by nearest neighbors (Fig. 3 a)). Similarly, a trigonal field alone (C_{3v} symmetry) splits the 4d-orbitals into a singlet (C0) and two doublets (C1, C2). These observations

can be directly obtained from group theory [20].

Terms E_{Od}, E_{Ot}, and E_{C0}, E_{C1}, E_{C2} give the differences in energy from the free ion state due to the cubic and trigonal fields, respectively. Fig. 3 b) illustrates a situation where the trigonal field has a stronger influence than the cubic, and the choice of parameters here (see values in A, Table 4) is such that the lowest and highest states depicted are two doublets, while the middle state is a singlet. This is based on previous work [22], [23], where it is argued that spatial confinement due to nearest neighbors along the crystal's c-axis is particularly important in deciding the order of the energy states. The singlet state has a strong Y_2^0 component that is highly symmetric along the c-axis. The distance from the defect to the nearest atom along the c-axis depends on the type of site it occupies (h, k_1, k_2). Thus, considering Coulomb interaction along the c-axis for a defect at an h-site, the singlet state lies in between the two doublets, whereas at a $k_{1,2}$-site, the singlet has a higher energy than the two doublets.

3.3 Spin-orbit coupling

Since the crystal fields alone do not act on the spin degree of freedom, we could so far model the system disregarding the spin degeneracy. When introducing spin-orbit coupling, however, the spin has to be taken into account. The SOC Hamiltonian is given as:

$$H_{soc} = \lambda \vec{\mathbf{L}} \cdot \vec{\mathbf{S}} \tag{2}$$

where λ gives the overall coupling strength in units of energy, and $\vec{\mathbf{L}}$, $\vec{\mathbf{S}}$ are the orbital angular momentum and spin operators, respectively, in vector form. This Hamiltonian is diagonal in the set of coupled basis states $|l\, s\, j\, m_j\rangle$, with $j = l + s = \frac{5}{2}$, but can be easily transformed into the decoupled basis $|m_l\, m_s\rangle$ via Clebsch-Gordan coefficients (see B, table 5). Fig. 3 c) illustrates the effect of weak spin-orbit coupling (when compared to the crystal fields). It can be seen (magnified in Fig 3 c)-ii)) how SOC further lifts the remaining two-fold orbital degeneracies, such that the system under consideration now consists of five separate spin-orbital doublets, labeled by increasing energy. These doublets, called Kramers doublets, show Kramers degeneracy, which will be further explored in the next section.

3.4 Kramers degeneracy

The two-fold degeneracy of Kramers doublets (KD) is a consequence of time-reversal invariance [21]. States in a doublet are each other's time-reversed version such that, in the presence of time-reversal symmetry, they must be degenerate. Neither the crystal field, nor the SOC Hamiltonians break time-reversal symmetry. However, the presence of an external magnetic field does break time-reversal symmetry, such that this two-fold degeneracy can be lifted. Thus, when an external magnetic field is applied, the original doublet splits into two branches, and the splitting increases proportionally with the field. It follows that the behavior of each KD under the action of a

magnetic field can be described by an effective spin Hamiltonian for the Zeeman interaction:

$$\tilde{H}_{Zee} = -\frac{\mu_B}{\hbar}\vec{B}\cdot\mathbf{g}\cdot\vec{\tilde{\mathbf{S}}} \tag{3}$$

with μ_B - Bohr magneton, $\vec{B}$ - applied magnetic field vector, $\mathbf{g}$ - g-factor tensor, $\vec{\tilde{\mathbf{S}}}$ - effective spin operator in vector form. The tilde refers to effective operators. The g-tensor is then a phenomenological parameter describing how the energy splitting between the two effective spin states evolves as a function of magnetic field strength. For the ground state of the Mo defect, this energy splitting is non-zero only when $\vec{B} \parallel \hat{c}$.

The energy splitting of the effective spin-1/2 states due to a field $\vec{B} \parallel \hat{c}$ is given as $\Delta E = \mu_B B_{\parallel} g_{\parallel}$. The proportionality constant is thus $\mu_B g_{\parallel}$, where in effect $g_{\parallel}$ couples the applied field with the spin described by an effective operator $\tilde{\mathbf{S}}_z$. The KDs can then be labeled according to the eigenstates of $\tilde{\mathbf{S}}_z$, as spin-up and spin-down states, $|KD\uparrow\rangle, |KD\downarrow\rangle$.

This phenomenological description can be used to extract information at a macroscopic scale, but differs from the description of real, microscopic spins and their interactions. This is presented in the following chapters.

4 Hamiltonian of the defect

Our goal is to relate the effective spin Hamiltonian to the first principles model of the interactions discussed so far. In doing so, we confirm its validity and gain further understanding on the conditions of its validity.

The three intrinsic interactions discussed - cubic and trigonal crystal fields, SOC - are additive, and, for a static crystalline configuration, they are captured by a total Hamiltonian H_0:

$$H_0 = H_{T_d} + H_{C_{3v}} + H_{soc} \tag{4}$$

Each term in the above relation must be transformed into a common $|m_l\, m_s\rangle$ representation (see cubic-spherical harmonics relations 53, CG coefficients table 5). The quantization axis of l, s is along the C_3 symmetry axis of the defect. In this way, the states whose energies are shown in Fig. 3 and which we are interested in characterizing, are linear combinations of the decoupled basis states $|m_l\, m_s\rangle$. Mathematically, these states are eigenstates of the H_0 Hamiltonian, given below in block matrix form, and the corresponding energies are its eigenvalues.

$$H_0 \quad = \quad \begin{pmatrix} B_1 & 0 & 0 \\ 0 & B_2 & 0 \\ 0 & 0 & B_3 \end{pmatrix}$$

with blocks

$$B_1 \quad = \quad B_2 = \begin{pmatrix} \lambda + \frac{1}{3}(3E_{C2} + E_{Od} + 2E_{Ot}) & -\frac{\sqrt{2}i}{3}(E_{Od} - E_{Ot}) & 0 \\ \frac{\sqrt{2}i}{3}(E_{Od} - E_{Ot}) & -\frac{\lambda}{2} + \frac{1}{3}(3E_{C1} + 2E_{Od} + E_{Ot}) & \frac{\sqrt{6}\lambda}{2} \\ 0 & \frac{\sqrt{6}\lambda}{2} & E_{C0} + E_{Ot} \end{pmatrix}$$

$$B_3 \quad = \quad \begin{pmatrix} \frac{\lambda}{2} + \frac{1}{3}(3E_{C1} + 2E_{Od} + E_{Ot}) & \frac{\sqrt{2}i}{3}(E_{Od} - E_{Ot}) & \lambda & 0 \\ -\frac{\sqrt{2}i}{3}(E_{Od} - E_{Ot}) & -\lambda + \frac{1}{3}(3E_{C2} + E_{Od} + 2E_{Ot}) & 0 & \lambda \\ \lambda & 0 & -\lambda + \frac{1}{3}(3E_{C2} + E_{Od} + 2E_{Ot}) & -\frac{\sqrt{2}i}{3}(E_{Od} - E_{Ot}) \\ 0 & \lambda & \frac{\sqrt{2}i}{3}(E_{Od} - E_{Ot}) & \frac{\lambda}{2} + \frac{1}{3}(3E_{C1} + 2E_{Od} + E_{Ot}) \end{pmatrix}$$

written in the ordered basis $|m_l\, m_s\rangle$:

$$\begin{aligned} B_1 \quad &\rightarrow \quad \left\{ |2, \frac{1}{2}\rangle, |-1, \frac{1}{2}\rangle, |0, -\frac{1}{2}\rangle \right\} \\ B_2 \quad &\rightarrow \quad \left\{ |-2, -\frac{1}{2}\rangle, |1, -\frac{1}{2}\rangle, |0, \frac{1}{2}\rangle \right\} \\ B_3 \quad &\rightarrow \quad \left\{ |1, \frac{1}{2}\rangle, |-2, \frac{1}{2}\rangle, |2, -\frac{1}{2}\rangle, |-1, -\frac{1}{2}\rangle \right\} \end{aligned} \tag{5}$$

The parameters of H_0 presented in subsection 3.2, and used to obtain the energy diagram in Fig. 3 were chosen to approximately fit the observed experimental features of Mo and V defects, in order of magnitude. These defects show two closely spaced KDs (energy difference $\approx$ 1 meV), and an optically excited state that is $\approx$ 1 eV higher in energy (see A, Table 4).

4.1 Dimensionality of the full Hilbert space

The hyperfine coupling energy observed for these defects [12] is orders of magnitude smaller than the crystal fields' or that of the SOC, such that nothing changes in energy configuration at the level of coarseness we are now considering. Although one may choose to ignore the nuclear spin for now, we choose to work in the full basis set that includes the nuclear spins from the start. When taking into account the nuclear spin effect we must expand the basis states space to $\{|m_l\, m_s\, m_i\rangle\}$, in order to contain all eigenstates. For the Mo defect with non-zero nuclear spin, $i = \frac{5}{2}$, and so $m_i = -\frac{5}{2}, -\frac{3}{2}, ..., \frac{5}{2}$. Thus, whereas the Hilbert space spanned by $|m_l\, m_s\rangle$ is only 10-dimensional, the one spanned by the basis states $|m_l\, m_s\, m_i\rangle$ is 60-dimensional.

4.2 Visualization of high-dimensional matrices

For obvious reasons, the 60-dimensional space is much less tractable than the 10-dimensional one. We find that a good way to understand and visualize matrices in such a high-dimensional space is by using color maps like those shown in Fig. 4. Fig. 4a shows the H_0 Hamiltonian representation in the 10-dimensional basis that ignores the nuclear spins, while Fig. 4b illustrates the same Hamiltonian in the expanded 60-dimensional basis. The colored squares give the location and value of a matrix element of the form $\langle m_l'\, m_s'\, (m_i')|H_0|m_l\, m_s\, (m_i)\rangle$, in the ordered basis given in Eq. 5. Each square in the 10-dimensional representation corresponds to 6×6 squares in the 60-dimensional one. In performing the basis expansion, only matrix elements preserving the m_i-value are allowed to be non-zero; i.e., no mixing of different $|m_i\rangle$ states is allowed by H_0. This is in accordance with the fact that we have thus far not taken into account the hyperfine interaction.

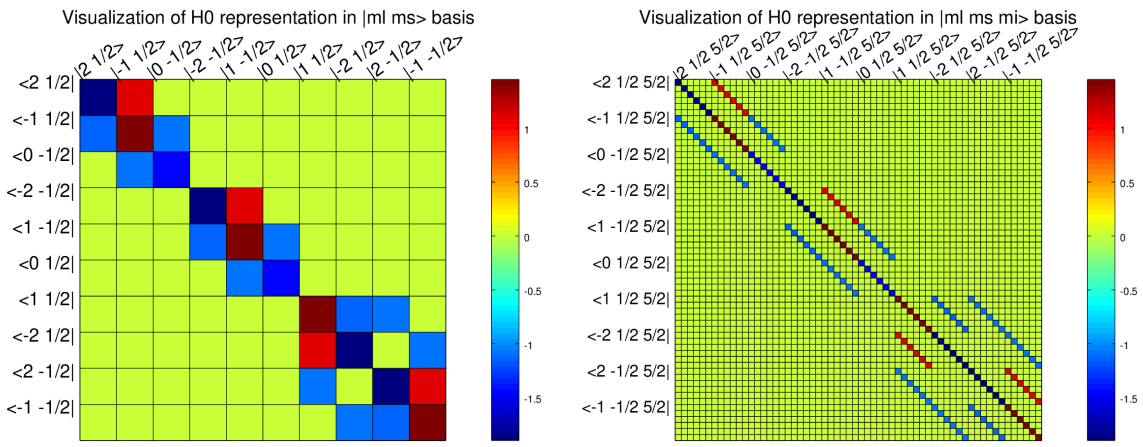

(a) (b)

Figure 4: Visual representation of the H_0 Hamiltonian in the basis $|ml\, ms\rangle$ (4a) and $|ml\, ms\, mi\rangle$ (4b), for $l = 2$, $s = \frac{1}{2}$, $i = \frac{5}{2}$. The quantization axis z coincides with the c-axis of the crystal. The basis states are ordered such that the Hamiltonian is in block diagonal form, rather than ordering them by energy. Thus, it is easy to see between which states interactions are symmetry-limited within each block. No mixing exists between states from different blocks. Within blocks, off-diagonal terms may appear which convey mixing between basis states. These are a result of crystal fields and spin-orbit coupling. A log-like scale is used here (for an explanation, see appendix C).

4.3 Eigenstates of $\mathbf{H_0}$

As already mentioned, the eigenstates of H_0 are linear combinations of basis states $|m_l\, m_s\, m_i\rangle$. Any such eigenstate, termed $|\psi\rangle$ can be written as:

$$\begin{aligned} |\psi\rangle &= \left(\sum_{k=1}^{60} |ml\, ms\, mi\rangle_{k\,k}\langle ml\, ms\, mi|\right) \cdot |\psi\rangle \\ &= \sum_{1}^{60} {}_k\langle ml\, ms\, mi|\psi\rangle |ml\, ms\, mi\rangle_k \end{aligned} \tag{6}$$

since $\sum_{k=1}^{60} |ml\, ms\, mi\rangle_{k\,k}\langle ml\, ms\, mi| = I$ is the identity operator for a complete, orthonormal basis set of dimension k. In eq. 6, the complex coefficients $\langle ml\, ms\, mi|\psi\rangle$ give the probability amplitude of an electron in state $|\psi\rangle$ to be found in the respective $|ml\, ms\, mi\rangle$ state.

When considering the nuclear spin degree of freedom, each of the KD energy states shown in Fig. 3 is 12-fold degenerate. Furthermore, within one KD, some of the eigenstates are labeled as carrying effective spin $|KD\uparrow\rangle$, and others as $|KD\downarrow\rangle$, according to their behavior under an applied magnetic field along the symmetry axis of the defect (see section 3.4).

Fig. 5 shows the probabilities $|\langle ml\, ms\, mi|\psi\rangle|^2$ for each set of eigenstates of KD 1-3 (5a, 5b, 5c, respectively). In these figures, each column is an eigenstate $|\psi\rangle$, labeled as $|KD\uparrow\rangle, |KD\downarrow\rangle$ and each row is a basis state, summed over $|m_i\rangle$ for simplicity. Then, both $|KD1\uparrow\rangle$ and $|KD3\downarrow\rangle$ are mixed states within the basis set B_1 in eq. 5. Similarly, $|KD1\downarrow\rangle$ and $|KD3\uparrow\rangle$ mix basis states of the set B_2. Finally, $|KD2\uparrow\rangle$ and $|KD2\downarrow\rangle$ are both mixed states belonging to the set B_3. This observation is closely related to the fact that H_0 is block diagonal.

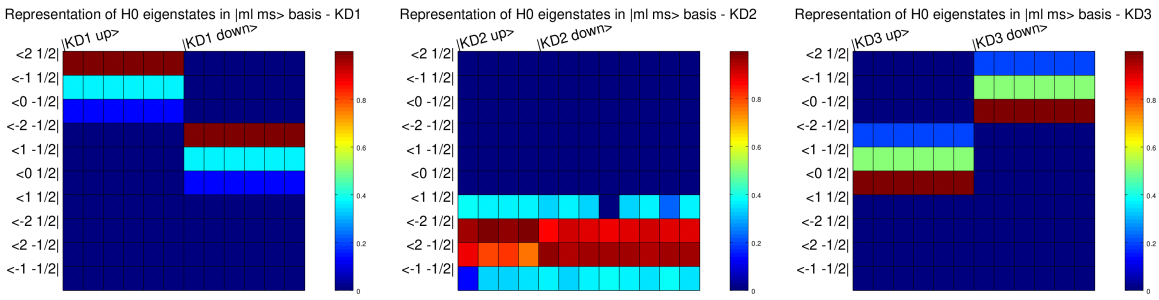

(a) (b) (c)

Figure 5: Composition of H_0 eigenstates in basis states $|m_l\, m_s\, m_i\rangle$, for KD1 (top), KD2 (middle) and KD3 (bottom). In this expansion, we sum over all 6 $|m_i\rangle$ values. The eigenstates are labeled by $|KD\uparrow,\downarrow\rangle$, depending on their behavior when an external magnetic field is applied (along the crystal c-axis). A log-like scale is used, in order to capture all non-zero probability coefficients (see appendix C). Within a figure, the columns represent eigenstates, and the rows represent basis states.

4.4 Effect of an external magnetic field

We now discuss the Zeeman interaction at the microscopic scale, where we consider the interaction of real electronic and nuclear spins with an external magnetic field. The Hamiltonian describing

this interaction is given in operator form as:

$$H_{Zee} = -\frac{\mu_B}{\hbar}\vec{B}\cdot(g_e\vec{\mathbf{S}} + k\vec{\mathbf{L}}) - \frac{\mu_N}{\hbar}\vec{B}\cdot g_p\vec{\mathbf{I}} \tag{7}$$

with μ_B is the Bohr magneton, $\vec{B}$ is the applied magnetic field vector, g_e is the electronic g-factor, $\vec{\mathbf{S}}$ is the electronic spin operator in vector form, $\vec{\mathbf{L}}$ is the electronic orbital angular momentum operator in vector form, μ_N is the nuclear magneton, g_p is the nuclear g-factor, and $\vec{\mathbf{I}}$ is the nuclear spin operator in vector form. The factor k effectively reduces the orbital angular momentum, due to wavefunction overlap between the Mo ion and its neighbors (see discussion in appendix D). The nuclear Zeeman interaction is three orders of magnitude weaker than the electronic Zeeman, given the mass difference between an electron and a nucleon. Since the crystalline c-axis is effectively a quantization axis, the vectors in eq. 7 are written in a coordinate system where $\hat{z} \parallel \hat{c}$, and the x, y-axes form the basal plane, $\hat{x}, \hat{y} \perp \hat{c}$.

4.4.1 Magnetic anisotropy

When analyzing the effects of this Hamiltonian on the energy configuration of spin states, we are focused on explaining the experimentally observed anisotropy in the Zeeman splitting.

For an applied parallel field (along the crystal c-axis), the Zeeman Hamiltonian in eq. 7 keeps the following terms:

$$H^z_{Zee} = -\frac{\mu_B}{\hbar}B_z\cdot(g_e\mathbf{S}_z + k\mathbf{L}_z) - \frac{\mu_N}{\hbar}B_z\cdot g_p\mathbf{I}_z \tag{8}$$

The effect of this Zeeman interaction can be easily visualized with a color map. Fig. 6a shows the distribution and relative value of matrix elements $|\langle KD_{H0}\uparrow,\downarrow|H^z_{Zee}|KD_{H0}\uparrow,\downarrow\rangle|$. These matrix elements represent the projection of the Zeeman Hamiltonian in the basis set of eigenstates of the H_0 Hamiltonian, labeled as the effective spin states $|\uparrow,\downarrow\rangle$ of the Kramers doublets. In the basis of effective spin-$\frac{1}{2}$ states of $KD1,3,5$, that is, within each 12×12 block matrix pertaining to these KDs, only diagonal matrix elements are non-zero. For the uniaxial symmetry type of this system, a parallel magnetic field may only couple to an effective spin operator $\tilde{\mathbf{S}}_z$, and this coupling is given by the g-tensor term g_{zz} (appendix E shows this in detail). In other words, the states $|KD1,3,5\uparrow,\downarrow\rangle$ are simultaneous eigenstates of H_0 and H^z_{Zee}. This is not the case for states $|KD2,4,\uparrow,\downarrow\rangle$, where (some) off-diagonal terms are non-zero as well. The quantization axis of these effective spin states does not coincide with the z-axis, and the effective g-tensor will have non-zero off-diagonal terms g_{zx}, g_{zy} that couple the magnetic field to effective spin operators $\tilde{\mathbf{S}}_x, \tilde{\mathbf{S}}_y$, respectively. Irrespective of which terms (diagonal or off-diagonal) of the g-tensor are non-zero, their presence on the color map indicates that an energy splitting can be observed for all Kramers doublets (KD1-KD5), when applying a magnetic field along the z-axis (where $\hat{z} \parallel \hat{c}$).

The energy diagram in Fig. 6b shows this expected splitting. Compared with the energies due to Hamiltonian H_0 alone, shown in part a), a magnetic field of 400 mT in the z-direction, $B_z = 400$ mT, causes the five KDs to split by an amount $\frac{\Delta E}{2}$ from their initial value; that is, the energies of

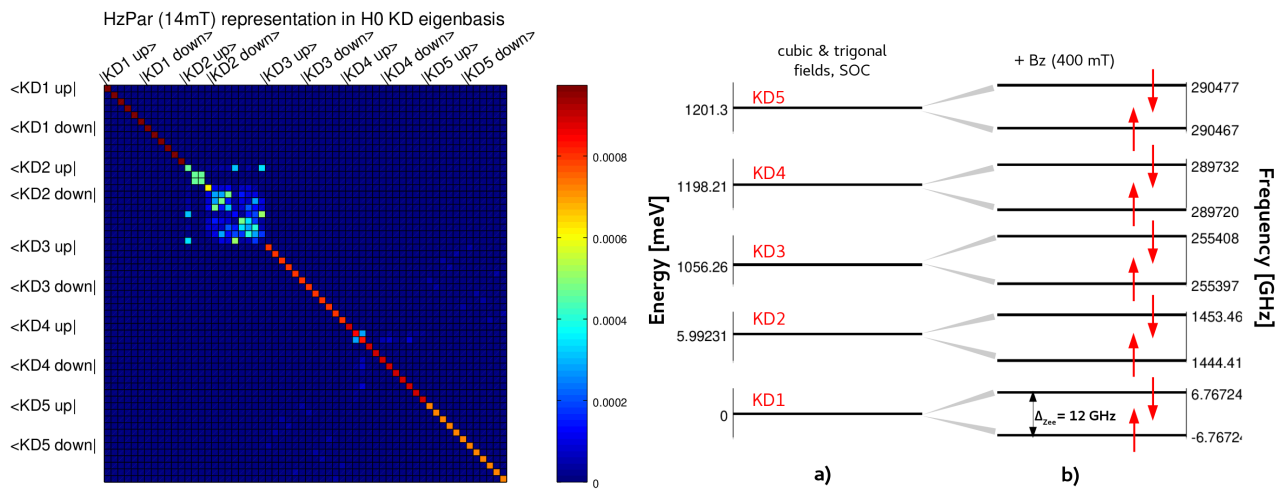

(a) (b)

Figure 6: 6a: Projection of H^z_{Zee} in the basis of H_0 eigenstates, for a field strength of 14 mT. The values of norms of matrix elements are given on a color scale. 6b: Energy splitting due to $H_0 + H^z_{Zee}$. a) Before applying the field the KDs are only described by H_0. b) Once a 400 mT field is applied, the KDs split into effective spin states $|KD\uparrow,\downarrow\rangle$, with energy difference $\approx$ 12 GHz. These effective states are further split due to the nuclear Zeeman interaction which is not visible in the diagram, due to the relative strength difference between the electronic and nuclear Zeeman components of H^z_{Zee}.

the two spin states in each KD are now $E_{1,2} = E_{H_0} \mp \frac{\Delta E}{2}$. The splitting $\Delta E = E_2 - E_1$ is given on a frequency scale and varies between 9-12 GHz depending on the KD. Due to the much smaller contributon of the nuclear Zeeman interaction, this cannot be resolved in Fig. 6b.

For a field applied in the basal plane ($\vec{B} \perp \hat{c}$), the Zeeman Hamiltonian in eq. 7 reduces to:

$$H^x_{Zee} = -\frac{\mu_B}{\hbar} B_x \cdot (g_e \mathbf{S}_x + k\mathbf{L}_x) - \frac{\mu_N}{\hbar} B_x \cdot g_p \mathbf{I}_x \tag{9}$$

$$= -\frac{\mu_B}{\hbar} B_x \cdot \left(g_e \left(\frac{\mathbf{S}_+ + \mathbf{S}_-}{2} \right) + k \left(\frac{\mathbf{L}_+ + \mathbf{L}_-}{2} \right) \right) - \frac{\mu_N}{\hbar} B_x \cdot g_p \left(\frac{\mathbf{I}_+ + \mathbf{I}_-}{2} \right) \tag{10}$$

where we write the Hamiltonian in terms of angular momentum ladder operators. As before, we show in Fig. 7a the norms of matrix elements $|\langle KD_{H0}\uparrow,\downarrow|H^x_{Zee}|KD_{H0}\uparrow,\downarrow\rangle|$. From the constraints set by uniaxial symmetry, a magnetic field along the x-axis may only couple to an effective spin operator $\tilde{\mathbf{S}}_x$, with coupling strength given by the g-tensor term g_{xx}. In the basis of effective spin-$\frac{1}{2}$ states quantized along the defect's symmetry axis, $g_{xx} \neq 0$ would give terms on the off-diagonals; i.e. terms that couple KD states of opposite effective spin. In the above figure, one can see that for $KD1, 2, 4, 5$, all matrix elements within the 12×12 block matrices corresponding to each KD are zero, and we may conclude that $g_{xx} = 0$. Since there are no non-zero matrix elements of the real spin Zeeman Hamiltonian that couple $|KD\uparrow\rangle$ to $|KD\downarrow\rangle$, we expect no observable splitting of energy states for these KDs. For KD3, there are both diagonal and off-diagonal non-zero matrix elements. This can be interpreted as a departure from uniaxial symmetry, such that the effective g-tensor will have non-zero off-diagonal terms g_{xy}, g_{xz} that couple the magnetic field $\vec{B} \parallel \hat{x}$ to effective spin operators $\tilde{\mathbf{S}}_y, \tilde{\mathbf{S}}_z$, respectively. These non-zero terms indicate that an energy

splitting can be observed for KD3 when applying a magnetic field along the x-axis (where $\hat{x} \perp \hat{c}$).

The energy diagram in Fig. 7b shows this expected behavior. Compared with the energies due to Hamiltonian H_0 alone, shown in part a), a magnetic field of 400 mT in the x-direction, $B_x = 400$ mT, causes the two lowermost and two highermost KDs to split by a small amount $\Delta E = 0.085$ GHz, due to the nuclear Zeeman interaction. The splitting $\Delta E = 11$ GHz observed for KD3 is due to the much stronger electronic Zeeman interaction, and we can therefore assign the lower energy state to an effective $|\uparrow\rangle$ spin state, and the higher energy state as corresponding to an effective $|\downarrow\rangle$ spin state.

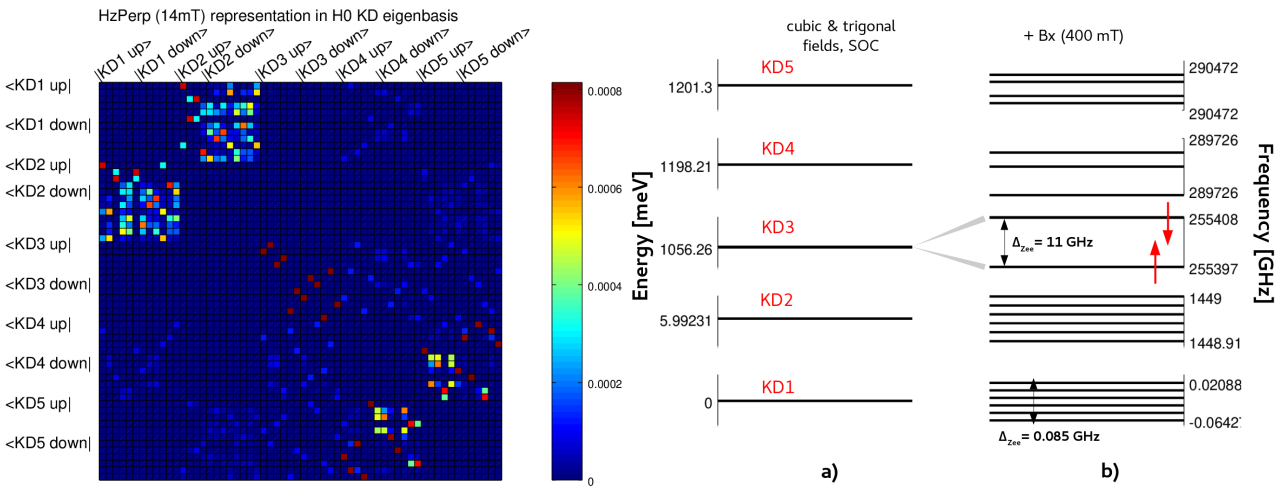

(a) (b)

Figure 7: 7a: Visual representation of H^x_{Zee} in the basis $|KD_{H_0} \uparrow, \downarrow\rangle$, for a field of strength 14 mT in the basal plane. The values of norms of matrix elements are given on a color scale. 7b: Energy splitting due to $H_0 + H^x_{Zee}$. a) Before applying the field the KDs are only described by H_0. b) Once a 400 mT field is applied, KDs 1-2 and 4-5 split into bands of ≈ 0.085 GHz due to nuclear Zeeman interaction. KD3 further splits into effective spin states $|KD \uparrow, \downarrow\rangle$ due to electronic Zeeman interaction.

The behavior seen in Figs. 6, 7 can be explained in conjunction with Fig. 5. Applying the operators $\mathbf{S}_z, \mathbf{L}_z$, or $\mathbf{I}_z$ to states of $|KD1 \uparrow\rangle$, for example, which consist in a large proportion of basis states $|2\,\frac{1}{2}\,m_i\rangle$, will bring us back to the same set of $|2\,\frac{1}{2}\,m_i\rangle$ states. This can be extrapolated to other KDs whose effective spin $|\uparrow, \downarrow\rangle$ states consist of non-overlapping subsets of basis states $|m_l\, m_s\, m_i\rangle$. KD2 does not fulfill this condition: its effective spin $|\uparrow, \downarrow\rangle$ states are composed of the same subset of basis states. Acting with the diagonal real spin operators $\mathbf{S}_z, \mathbf{L}_z$, $\mathbf{I}_z$ can bring us from an effective spin $|\downarrow\rangle$ state to an effective spin $|\uparrow\rangle$ state or vice versa.

Acting with the ladder operators $\mathbf{S}_\pm, \mathbf{L}_\pm$ on the basis states $|2\,\frac{1}{2}\,m_i\rangle, |-2\,-\frac{1}{2}\,m_i\rangle$ of KD1 brings them onto basis states $|2\,-\frac{1}{2}\,m_i\rangle, |-2\,\frac{1}{2}\,m_i\rangle, |1\,\frac{1}{2}\,m_i\rangle, |-1\,-\frac{1}{2}\,m_i\rangle$. KD1 does not contain these states and the energy difference between different KDs due to spin-orbit coupling is much larger than that due to the Zeeman interaction within one KD. Thus, the energy splittings are very small, and only due to the effect of ladder operators $\mathbf{I}_\pm$ on the $|m_i\rangle$ basis states. In the case of KD3, whose effective spin states $|KD3 \uparrow\rangle, |\downarrow\rangle$ contain strong components of $|0\,\frac{1}{2}\,m_i\rangle, |0\,-\frac{1}{2}\,m_i\rangle$ basis states, respectively, the ladder operators can couple the two opposite effective spin states.

4.4.2 Calculated g-factor

We extract g-factor values from the energy splittings of the modeled Zeeman interaction given that:

$$\Delta E_{Zee} = \mu_B B g \tag{11}$$

for $\Delta E_{Zee} = E_1 - E_2$, where $E_{1,2}$ are the eigenvalues of Hamiltonian $H_0 + H_{Zee}$. In Table 1 we show values of the g-factor calculated based on the splittings observed in Figs. 6b, and 7b. For comparison, we summarize the values extracted from measurements on Mo in 6H-SiC in [13], as well as from measurements on V in 6H-SiC, [12].

Table 1: Theoretical g-factor values extracted for KD1-KD3 from splittings shown in Figs. 6b, and 7b. Experiment Mo: g-factor values extracted for the ground state (GS) and optically excited state (ES) of the Mo^{5+} defect at an h-site in 6H-SiC from measurements by T. Bosma et al. [13]. Experiment V: g-factor values extracted for the ground states (GS1-2) and optically excited state (ES1) of the V^{4+} defect at a k_2-site in 6H-SiC from measurements by G. Wolfowicz et al. [12].

	Theory			Experiment Mo		Experiment V		
	KD1	KD2	KD3	GS	ES	GS1	GS2	ES1
g_z	2.1434	1.6076	1.9648	1.61 ± 0.02	1.20 ± 0.02	1.933(5)	1.972(5)	2.03(2)
g_x	0.015183	0.016076	1.9648	0.000 ± 0.004	0.11 ± 0.02	$0 < g < 1$	$0 < g < 1$	-

The choices of parameters for the H_0 Hamiltonian, and the reduction factor k influence the values of calculated g-factors. Since H_0 was modeled on the assumption that the Mo defect is at a Si substitutional h-site, we start the comparison of calculated versus measured g-factors for this defect. KD1 and KD2, modeled as ground states, show very different g_z values. Whereas g_z^{KD1} is larger than the experimentally measured g_z^{GS}, g_z^{KD2} is within the measured value's uncertainty range. The g_x-values of the lowermost KDs given in the above table correspond to the largest possible splitting; that is, the full width of the band due to the closely spaced states split by the nuclear Zeeman interaction. Considering smaller splittings within this band gives a range of (approximate) values, $g_x \in [0.003, 0.015]$. From this, it can be concluded that states describing KD2 in our model are similar to the actual ground state of the Mo defect. A similar direct comparison can be made between KD3 and the optically excited state called ES. For this state, the theoretical and experimental g_z, g_x-values differ quite a lot. This KD contains the highest zero-orbital angular momentum component among the modeled KDs, such that tuning the g-factor via the orbital reduction factor k will not give a better match between calculated and measured g_z-values. It is then likely that KD3 does not correspond to the actual optically excited state. This could imply that the modeled order of KDs in terms of energies is incorrect, and further analyses of better suited crystal field parameters are needed to shed light on this.

Regarding the V defect, which lies at a Si substitutional k_2-site, and thus has a different next-nearest neighbor environment than the Mo defect, the discrepancy between our calculated g-values and the experimental ones is less large. In this case, tweaking the k-factor could give a better fit, at least for the ground states. For the optically excited state, for which a g_x-value could not be

resolved, it is not possible to say whether a different KD order would give a better fit.

4.4.3 Microwave driving

In section 2.2 we discussed the issue of spin control of these transition metal defects in SiC for quantum information technology applications. We can explore the possibility of spin control in the framework of the model of H_0, in conjunction with the anisotropic Zeeman interactions for real spins of eqs. 8, 9, and with reference to the electron spin resonance Hamiltonian in eq. 1. Applying a static field B_0^z will give a splitting in the energy states of the effective spins within each KD, as seen in the previous section. These effective spin states $|KD\uparrow,\downarrow\rangle$ are the eigenstates of total Hamiltonian $H_0 + H_{Zee}^z$ for B_0^z, and are labeled $|KD_{H_0+H_{Zee}^z}\uparrow,\downarrow\rangle$. The effect of a second applied magnetic field B_1, either parallel to the c-axis or in the basal plane, should then be considered in the basis of these eigenstates. This is illustrated by the color maps in Fig. 8.

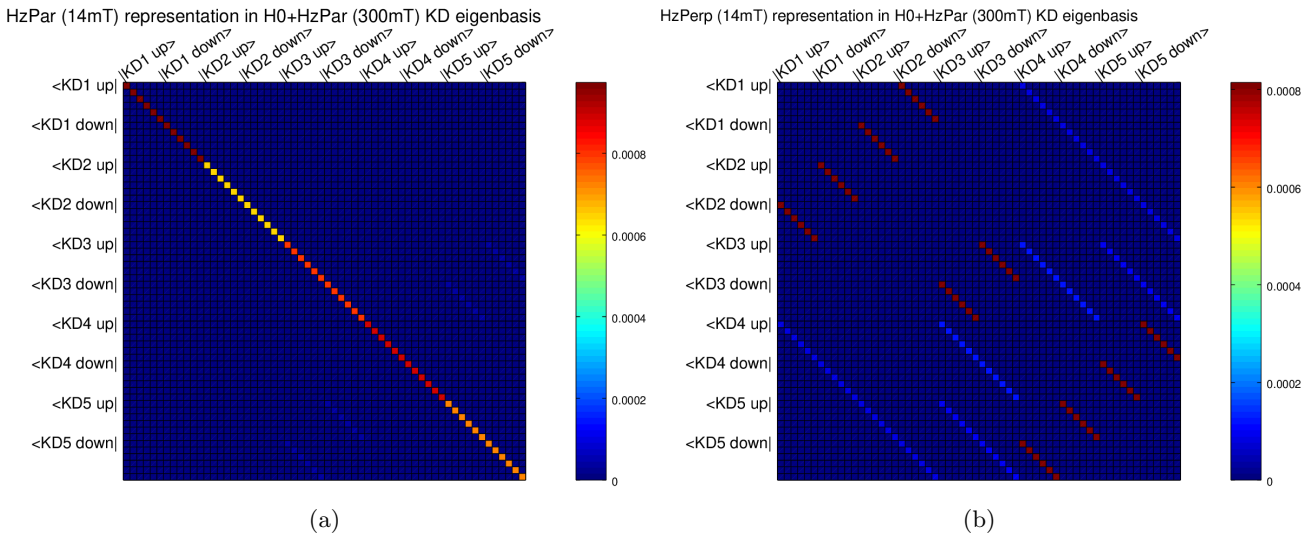

(a) (b)

Figure 8: Representation of $|\langle KD_{H_0+H_{Zee}^z}\uparrow,\downarrow|H_{Zee}|KD_{H_0+H_{Zee}^z}\uparrow,\downarrow\rangle|$ for a $H_{Zee} \equiv H_{Zee}^z$ (8a), and for a $H_{Zee} \equiv H_{Zee}^x$ (8b). The location and value of matrix elements in these pictures give an indication as to whether microwave driving of electronic spins is possible, via a dynamic magnetic field either along the crystal c-axis or in the basal plane. A static field of 300 mT in the parallel direction is chosen to lift the effective spin degeneracies. The dynamic field strength is 14 mT.

For the case of a dynamic field in the z-direction, $B_1^z = 14$ mT, shown in Fig. 8a, we only find non-zero terms on the diagonal of each KD block. This means that only same-effective spin states can be coupled by this field. We do see non-zero off-diagonal matrix elements between states belonging to different KDs. Specifically, driving opposite spins of KD3 and KD5 can be done, in principle, via a dynamic parallel magnetic field. However, considering the energy separation between these spin states due to crystal fields and SOC, this cannot be done using microwaves. In connection with the experimentally observed spin resonance using a dynamic parallel field for the V defect ([12]), we conclude that the current model with this choice of parameters cannot explain these observations.

Given a dynamic field in the x-direction, $B_1^x = 14$ mT, shown in Fig. 8b, we only find non-zero

matrix elements within KD3. Moreover, these are found between states of opposite effective spin, implying that driving spin resonance is possible for the states of this KD, via a perpendicular field. A mathematical picture of this situation involves the presence of a non-zero g_{xx} effective g-tensor term. This couples the magnetic field to effective spin operator $\tilde{\mathbf{S}}_x$ which allows mixing between states of opposite spin. The fact that this scenario is possible for KD3 only is closely tied to the strong zero-orbital angular momentum component of these states.

To conclude, this chapter has introduced a basic model of interactions expected for the electronic spin states of the Mo and V defects in 6H-SiC, also in the presence of external magnetic fields. We are able to model the observed anisotropic response to magnetic fields applied along the crystalline c-axis or perpendicular to it, although further analysis is necessary to get a better fit of the g-factor. We cannot explain experimental observations of MW driving via a parallel dynamic field based on this model which ignores interactions with nuclear spins. In the following chapter we expand the model to include these interactions.

5 Influence of nuclear spins

This chapter is dedicated to an analysis of the effects of the interaction with the Mo nucleus, via the hyperfine interaction, on the electronic spin states. These effects can be responsible for mixing various electronic spin states, leading to additional paths for magnetic field coupling. It has been suggested that the experimental control of a V spin in 4H-SiC arise due to the hyperfine coupling [12]. Gaining a fundamental understanding of the interplay between nuclear and electronic spins may also be interesting for future hybrid applications that combine a processing unit and memory registers in the same device.

5.1 Hyperfine interaction

The hyperfine interaction can be understood in terms of electric or magnetic multipole expansions, where the most important contributions are from magnetic dipole and electric quadrupole interactions. Here, we address the magnetic dipole interactions. The nucleus carrying a non-zero spin angular momentum can interact with the orbital motion of an electron revolving around it, as well as with the electronic spin. In the case of an electron in an open shell, these interactions occur solely due to the single, unpaired electron (see Ch. 6 in [24]). As discussed in previous chapters, the Mo defect in 6H-SiC has the electronic configuration $[Kr]4d^1$, i.e. it has a single valence electron in its d-orbitals that carries spin $s = \frac{1}{2}$. The Mo nucleus can carry spin given by quantum number $i = \frac{5}{2}$ or $i = 0$, depending on the isotope.

The hyperfine interaction Hamiltonian is given by:

$$H_{hf} = \vec{\mu_p} \cdot \frac{\mu_0}{4\pi} \frac{e\vec{\mathbf{L}}}{mr^3} + \frac{\mu_0}{4\pi} \frac{1}{r^3} \left(\vec{\mu}_e \cdot \vec{\mu}_p - 3 \frac{(\vec{\mu}_e \cdot \vec{r})(\vec{\mu}_p \cdot \vec{r})}{r^2} \right) - \frac{\mu_0}{4\pi} \frac{8\pi}{3} \vec{\mu}_e \cdot \vec{\mu}_p \delta(\vec{r}) \tag{12}$$

with $\vec{\mu}_e$, $\vec{\mu}_p$ the intrinsic magnetic moment of the electron and proton (which we use for labeling the nuclear magnetic moment), respectively. Furthermore, μ_0 is the vacuum permeability, e and m are the electronic charge and mass, respectively, $\vec{r}$ is the position vector of the electron, with origin at the nucleus, and $\vec{\mathbf{L}}$ is the vector of the electron's orbital angular momentum.

The first term in eq. 12 gives the coupling of the electronic orbital angular momentum to the nuclear spin, the second arises from dipole-dipole interaction between electronic and nuclear spins, and the third due to Fermi contact interaction. For d-orbitals, which have zero electronic density at the nucleus, the last term is zero. In operator form, and considering d-orbitals only, the Hamiltonian H_{hf} becomes:

$$H_{hf} = \frac{\mu_0}{4\pi} \frac{g_e \mu_B g_p \mu_N}{\hbar^2} \frac{1}{r^3} \left(\vec{\mathbf{I}} \cdot \vec{\mathbf{L}} + 3 \frac{(\vec{\mathbf{S}} \cdot \vec{r})(\vec{\mathbf{I}} \cdot \vec{r})}{r^2} - \vec{\mathbf{S}} \cdot \vec{\mathbf{I}} \right) \tag{13}$$

where g_e, g_p are the free electron and proton g-factors, μ_B, μ_N are the Bohr and nuclear magneton, respectively, $\hbar$ is the reduced Planck constant, and $\vec{\mathbf{S}}, \vec{\mathbf{I}}$ are vectors of the electronic and nuclear spin operators, respectively.

Furthermore, similarly to the spin-orbit coupling, the hyperfine interaction Hamiltonian is diagonal in the basis $|f\, m_f\rangle$ of total angular momentum $\mathbf{F} = \mathbf{I} + \mathbf{J}$ and needs to be transformed to the $|m_l\, m_s\, m_i\rangle$ basis via Clebsch-Gordan coefficients. As before, we can use a color map (Fig. 9) to visualize the effect of adding H_{hf} to H_0. The off-(block)diagonal terms due to the hyperfine interaction mix the various KDs. Our goal in this section is to check whether this mixing leads to any deviations from the observed $g = 0$ which leads to the impossibility of driving electron spin resonance.

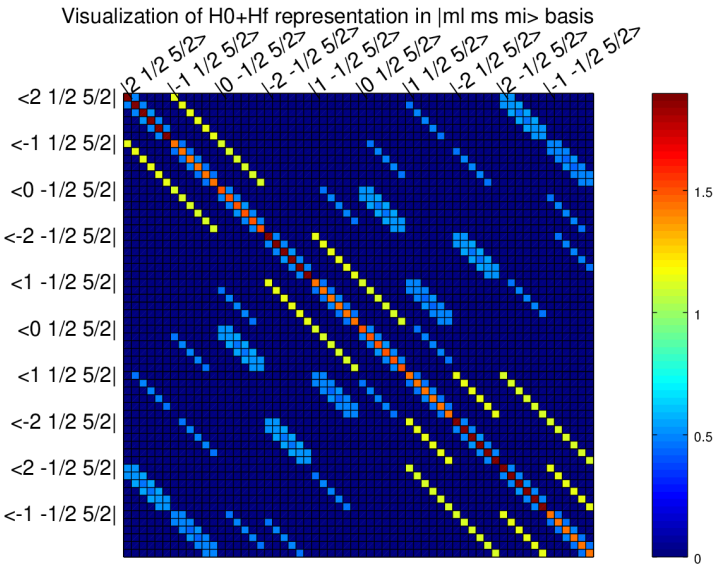

Figure 9: Visual representation of the $H_0 + H_{hf}$ Hamiltonian in the basis $|ml\, ms\, m_i\rangle$, for a hyperfine strength of 200 MHz. The ordering of basis states is unchanged from the block diagonal representation of H_0. When compared to the representation of H_0 alone, it is clear that off-diagonal terms do appear which are due to the hyperfine interaction. This gives mixing between basis states of opposite electronic or nuclear spin, with strength given on a log-like color scale (see appendix C).

5.2 Eigenstates and eigenvalues of $\mathbf{H}_0 + \mathbf{H}_{hf}$

The mixing of basis states $|ml\, ms\, mi\rangle$ due to the hyperfine interaction can be seen in Fig. 10. This illustrates the probabilities $|\langle ml\, ms\, mi|\psi\rangle|^2$ for each set of eigenstates of KD 1-3 (10a, 10b, 10c, respectively), arranged as a column and labeled as $|KD\uparrow\rangle, |KD\downarrow\rangle$. Each row is a basis state, summed over $|m_i\rangle$. We can compare this with the situation where we disregard the influence of nuclear spins, shown in Fig. 5. We see that the hyperfine interaction mixes states that previously strictly belonged to one or the other of the effective states $|KD\uparrow,\downarrow\rangle$, such that they now belong to both effective spin states. This is immediately clear for $|KD1\rangle$ and $|KD3\rangle$, whose $|\uparrow,\downarrow\rangle$ states are (almost) indistinguishable by their basis state composition. This is only apparently true, because we sum over $|m_i\rangle$ states. In reality, each eigenstate is composed of different (set of) nuclear spin states. In appendix H we include similar figures showing the full $|m_l\, m_s\, m_i\rangle$ contributions to the electronic spin states.

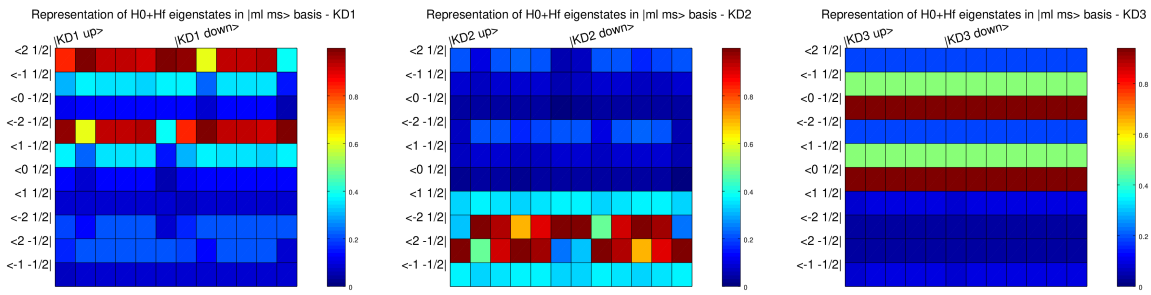

(a) (b) (c)

Figure 10: Composition of $H_0 + H_{hf}$ eigenstates in basis states $|m_l\, m_s\, m_i\rangle$, for KD1 (top), KD2 (middle) and KD3 (bottom). In this expansion, we sum over all 6 $|m_i\rangle$ values. The eigenstates are labeled by $|KD\uparrow,\downarrow\rangle$, depending on their behavior when an external magnetic field is applied (along the crystal c-axis). A log-like scale is used, in order to capture all non-zero probability coefficients (see appendix C). Within a figure, the columns represent eigenstates, and the rows represent basis states.

The hyperfine interaction necessarily changes the states we so far called Kramers 'doublets'. Because we chose to include the $|m_i\rangle$ basis from the start, when no nuclear spin interactions were considered, each KD was 12-fold degenerate. In the presence of an external magnetic field, the KDs split into electronic spin singlets. The nuclear Zeeman interaction lifts the nuclear spin degeneracy and thus prompts splitting within each electronic spin singlet. Nonetheless, since this splitting is very small, we could view each electronic spin singlet band as an effective electronic spin singlet. The hyperfine interaction lifts some of the degeneracies of the 12-fold degenerate KDs of H_0, even in the absence of a magnetic field. For this reason, we now view each KD defined under the action of H_0 as a Kramers doublet *band*. The manner in which the hyperfine interaction acts within each KD band to lift degeneracies is dependent on the eigenstates' composition shown in Fig. 10. For example, in the energy diagram illustrating eigenvalues of $H_0 + H_{hf}$ (Fig. 11b), we see 6 separate lines which correspond to the KD1 *band* (denoted here 'KD1'). It turns out that each of these 6 lines coresponds to a Kramers degenerate energy state. To name one example of such a state, we look closely at the eigenstate whose composition is illustrated in the second column of $|'KD1'\uparrow\rangle$ in Fig. 10. This eigenstate has a strong $|2\,\frac{1}{2}\,m_i\rangle$ (dark red) component, followed by a less strong $|-2\,-\frac{1}{2}\,m_i'\rangle$ (yellow) component ($m_i \neq m_i'$). Its time-reversal symmetric state has a strong $|-2\,-\frac{1}{2}\,-m_i\rangle$ (dark red) component, followed by a less strong $|2\,\frac{1}{2}\,-m_i'\rangle$ (yellow) component. This state can be found in the second column of $|'KD1'\downarrow\rangle$ of the same figure. The same can be said for the remaining states of 'KD1', as well as for those of 'KD2', and 'KD4'. 'KD3' is slightly different, in that each of its 12 states contains equally strong time-reversal symmetric states $|0\,-\frac{1}{2}\,m_i\rangle$ and $|0\,\frac{1}{2}\,-m_i\rangle$. 'KD5' has strong $|0\,\pm\frac{1}{2}\,m_i\rangle$ components as well, though not with equal weight within one eigenstate. Thus, to some extent, 'KD5' behaves like 'KD3'. For these reasons, these two 'KDs' show more than six separate lines in the energy diagram of $H_0 + H_{hf}$, since some of these energy levels correspond to singlets. For convenience, we continue to refer to these bands of six separate Kramers doublets (or several separate singlets) as (effective) KDs.

Even in the absence of an external magnetic field, the hyperfine interaction lifts the degeneracy

of $|m_i\rangle$ states. This can be observed experimentally if the technique, resolution and strength of the interaction are well matched. Fig. 11b shows the splitting in energy levels due to a hyperfine interaction strength of 200 MHz. The choice for this value was based on measurements on V^{4+} in SiC [12]. The splitting is mostly uniform within each KD, except for those KDs that contain strong $m_l = 0$ components, such as KD3, whose basis state composition is illustrated in Fig. 10c.

In modeling the hyperfine interaction, we tweak the prefactor in eq. 13:

$$\tau_{hf} = \frac{\mu_0 g_e \mu_B g_p \mu_N}{h \cdot 4\pi} \langle \frac{1}{r^3} \rangle \tag{14}$$

where h is Planck's constant, used to transform the prefactor into frequency units. We do this since we cannot determine the actual value of $\langle \frac{1}{r^3} \rangle$. However, this prefactor does not include the eigenvalues of operators in eq. 13, such that the actual hyperfine strength will differ per KD. The width of each KD band is given in Table 2, together with the effective hyperfine strength at play within each KD.

Table 2: Widths of KD band due to an input hyperfine interaction strength of 200 MHz. The actual effective strength for each KD varies, and is given as the average total band width divided by 5, for KD1-2 and KD4-5, which show more or less uniform splitting. For KD3, we give the effective hyperfine strength as a range from the smallest to the largest splitting.

KD	Band width (GHz)	Effective hyperfine strength (MHz)
1	0.67	133
2	1.02	204
3	1.01	0.6 - 456
4	0.51	102
5	0.33	67

5.3 Effect of an external magnetic field

The effect of magnetic field via the Zeeman interaction is investigated once more, following the same procedure as in subsection 4.4, taking into account that the eigenstates we address here contain mixing arising from the hyperfine interaction.

5.3.1 Magnetic anisotropy

For an external magnetic field along the crystalline c-axis, we plot the Hamiltonian H^z_{Zee} from eq. 8 in the basis of eigenstates of $H_0 + H_{hf}$. Fig. 11a shows norms of matrix elements $|\langle KD_{H_0+H_{hf}} \uparrow, \downarrow | H^z_{Zee} | KD_{H_0+H_{hf}} \uparrow, \downarrow \rangle|$. Compared to the elements $|\langle KD_{H0} \uparrow, \downarrow | H^z_{Zee} | KD_{H0} \uparrow, \downarrow \rangle|$ plotted in Fig. 6a, it appears that the Zeeman Hamiltonian in the new eigenbasis has new non-zero matrix elements. Within all five KDs, there are both diagonal and off-diagonal terms, and $|KD_{H_0+H_{hf}} \uparrow, \downarrow\rangle$ are not simultaneous eigenstates of $H_0 + H_{hf}$ and H^z_{Zee} since H_{hf} and H^z_{Zee} do not commute. From the composition of KD1, KD2 and KD3 in Fig. 10 it follows that acting with operators $\mathbf{S}_z$, $\mathbf{L}_z$, and $\mathbf{I}_z$ can bring us back to the same or the opposite effective spin state with non-zero probability.

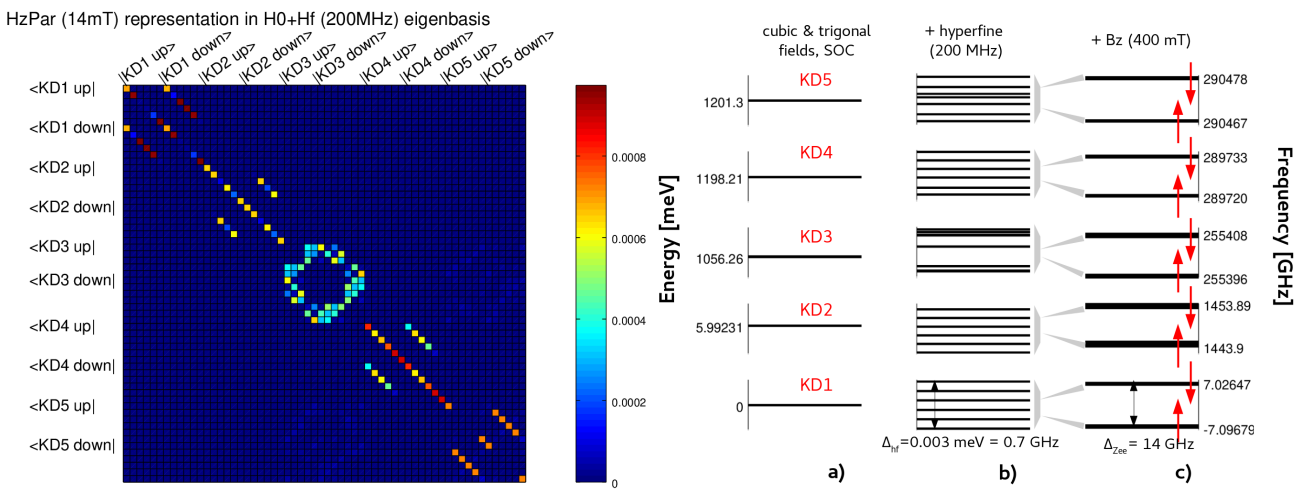

(a) (b)

Figure 11: 11a: Projection of H^z_{Zee} in the basis of $H_0 + H_{hf}$ eigenstates, for a field strength of 14 mT. The values of norms of matrix elements are given on a color scale. 11b: Energy splitting due to $H_0 + H_{hf} + H^z_{Zee}$, for $\vec{B} \parallel \hat{c}$. Before considering the hyperfine interaction or applying a magnetic field, the KDs are only described by H_0, shown in a). In b), a hyperfine interaction of strength 200 MHz is considered, which gives a splitting within the KD1 band of width ≈ 0.7 GHz (see table 2 for splitting within each KD). Once a 400 mT field is applied along the crystal c-axis, all KDs split into two branches, between 10-14 GHz apart, depending on the KD considered. These effective spin states are further split due to the nuclear Zeeman interaction which is not visible in the diagram, due to the relative strength difference between the electronic and nuclear Zeeman components of H^z_{Zee}.

In Fig. 11b c), we show the result of applying a static field $B_z = 400$ mT. For each effective KD, we observe a large splitting into so-called effective spin states $|\uparrow,\downarrow\rangle$. Each of these contains several (usually 6) eigenstates of $H_0 + H_{hf}$ slightly split by the hyperfine interaction. We choose this magnetic field strength in order to have a hierachy of interactions: $H_{Zee}(electronic) >> H_{hf} > H_{Zee}(nuclear)$.

Similarly, for an external magnetic field in the basal plane, we plot the Hamiltonian H^x_{Zee} from eq. 9 in the basis of H_0+H_{hf} eigenstates. Fig. 12a shows norms of matrix elements $|\langle KD_{H_0+H_{hf}} \uparrow,\downarrow|H^x_{Zee}|KD_{H_0+H_{hf}} \uparrow,\downarrow\rangle|$. Compared to the elements $|\langle KD_{H0} \uparrow,\downarrow|H^x_{Zee}|KD_{H0} \uparrow,\downarrow\rangle|$ plotted in Fig. 7a, the Zeeman Hamiltonian in the new eigenbasis has all-zero elements within KD1-2 and KD4-5, and some new non-zero matrix elements within KD3. This can be explained with the composition of KD3 in Fig. 10c. There are now more possibilities for the ladder operators to mix states of either the same or opposite effective spin states.

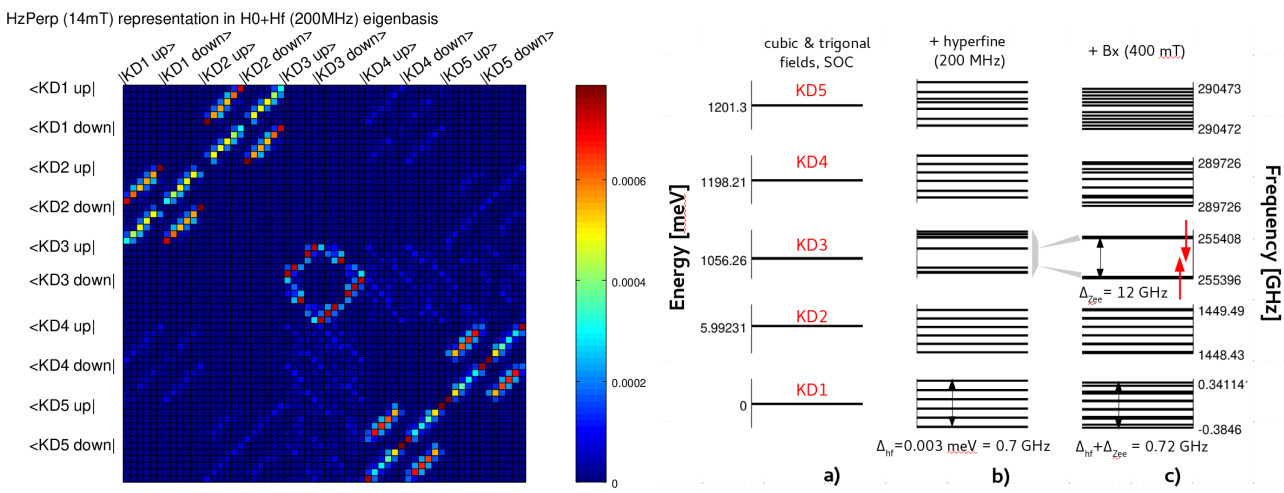

(a) (b)

Figure 12: 12a: Visual representation of H^x_{Zee} in the basis $|KD_{H_0+H_{hf}} \uparrow,\downarrow\rangle$, for a field of strength 14 mT in the basal plane. The values of norms of matrix elements are given on a color scale. 12b: Energy splitting due to $H_0 + H_{hf} + H^x_{Zee}$, for $\vec{B} \perp \hat{c}$. Before considering the hyperfine interaction or applying a magnetic field, the KDs are only described by H_0, shown in a). In b), a hyperfine interaction of strength 200 MHz is considered, which gives a splitting within a band of width ≈ 0.7 GHz. For a field applied in the basal plane in c), KDs 1-2 and 4-5 do not display a splitting. Rather, a small shift of some of the states is visible, due to the nuclear Zeeman interaction. KD3 does split into effective spin states $|KD3 \uparrow,\downarrow\rangle$ due to the electronic Zeeman interaction.

As expected from the values of matrix elements $|\langle KD_{H_0+H_{hf}} \uparrow,\downarrow |H^x_{Zee}| KD_{H_0+H_{hf}} \uparrow,\downarrow\rangle|$, there is no large splitting in Fig. 12b due to the electronic Zeeman interaction for KD1-2, and KD4-5. KD3 does show a large splitting due to the electronic Zeeman interaction, such that the effect of the hyperfine and nuclear Zeeman interactions cannot be resolved.

5.3.2 Calculated g-factor

As before, we can extract a theoretical effective g-factor from the splittings in Figs. 11b, and 12b. These are calculated for the maximum observed splittings and shown in Table 3. Compared with the g-factor values in Table 1, these values are larger, owing to the splitting due to the hyperfine interaction.

Table 3: Theoretical g-factor values extracted for KD1-KD3 from splittings shown in Figs. 11b, and 12b. Experiment Mo: g-factor values extracted for the ground state (GS) and optically excited state (ES) of the Mo^{5+} defect at an h-site in 6H-SiC from measurements by T. Bosma et al. [13]. Experiment V: g-factor values extracted for the ground states (GS1-2) and optically excited state (ES1) of the V^{4+} defect at a k_2-site in 6H-SiC from measurements by G. Wolfowicz et al. [12].

	Theory			Experiment Mo		Experiment V		
	KD1	KD2	KD3	GS	ES	GS1	GS2	ES1
g_z	2.5007	1.7862	2.1434	1.61 ± 0.02	1.20 ± 0.02	1.933(5)	1.972(5)	2.03(2)
g_x	0.12503	0.17862	2.1434	0.000 ± 0.004	0.11 ± 0.02	$0 < g < 1$	$0 < g < 1$	-

5.3.3 Microwave driving

We now re-explore the possibility of spin control in the framework of the model of $H_0 + H_{hf}$, in conjunction with the anisotropic Zeeman interactions for real spins of eqs. 8, 9, and with reference to the electron spin resonance Hamiltonian in eq. 1. We choose a static field B_0^z to split all effective KD spin states. These effective spin states $|KD\uparrow,\downarrow\rangle$ are now the eigenstates of total Hamiltonian $H_0 + H_{hf} + H_{Zee}^z$ for B_0^z, and are labeled $|KD_{H_0+H_{hf}+H_{Zee}^z}\uparrow,\downarrow\rangle$. We then consider the effect of a second applied magnetic field B_1, either parallel to the c-axis or in the basal plane, in the basis of these eigenstates. This is illustrated by the color maps in Fig. 13.

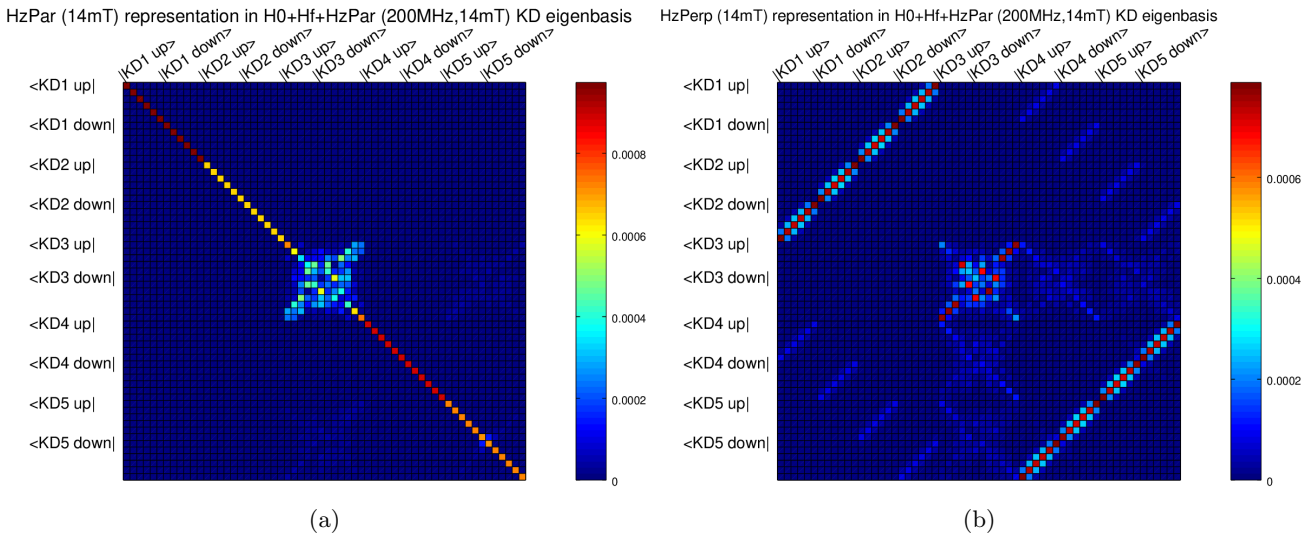

(a) (b)

Figure 13: Representation of $|\langle KD_{H_0+H_{hf}+H_{Zee}^z}\uparrow,\downarrow|H_{Zee}|KD_{H_0+H_{hf}+H_{Zee}^z}\uparrow,\downarrow\rangle|$ for a $H_{Zee} \equiv H_{Zee}^z$ (13a), and for a $H_{Zee} \equiv H_{Zee}^x$ (13b). The location and value of matrix elements in these pictures give an indication as to whether microwave driving of electronic spins is possible, via a dynamic magnetic field either along the crystal c-axis or in the basal plane. A static field of 14 mT in the parallel direction is chosen to lift the effective spin degeneracies. The dynamic field strength is 14 mT.

For the case of a dynamic field in the z-direction, $B_1^z = 14$ mT, shown in Fig. 13a, we only find terms that are non-zero in the diagonal for the KD1, KD2 and KD4 blocks. As explained in subsection 4.4.3, this means that the field dynamically changes the energies of the effective spin eigenstates, but cannot cause a transition between spins $\uparrow\downarrow$. However, for KD3 and, to a lesser extent, KD5, we also see non-zero off-diagonal terms. Mathematically, the effective g-tensor is allowed to have non-zero terms g_{zx}, g_{zy}, g_{zz} which couple the magnetic field B_1^z to each of the effective spin operators $\tilde{\mathbf{S}}_{z,x,y}$. Since $\tilde{\mathbf{S}}_{x,y}$ do mix states of opposite spin, it is possible to drive transitions between states of opposite spin with a parallel dynamic field. This can explain the experimentally observed spin resonance using a dynamic parallel field for the V defect ([12]). We can therefore conclude that these observations are due to the hyperfine interaction. Future experiments on the Mo defect that show a similar possibility for driving spin resonance via a parallel magnetic field will determine whether the model employed here is correct and whether it needs to be expanded to include interactions of higher orders.

Given a dynamic field in the x-direction, $B_1^x = 14$ mT, shown in Fig. 13b, we again only find non-zero matrix elements within KD3. We then conclude that driving spin resonance is possible for the states of this KD, via a perpendicular field.

The ability to drive electron spin resonance with either a parallel or a perpendicular field for eigenstates of KD3 and of KD5 arises from the fact that the Hamiltonian H_0 mixes basis states $|0 \pm \frac{1}{2}\, m_i\rangle$ into these eigenstates. Thus, terms in H_0 that mix these basis states into various other KDs can also elicit this response.

6 Conclusions and outlook

In this work we employed a theoretical model using first-principles techniques to understand the Mo and V defects in a polytype of SiC (6H-SiC). The model contains influences of crystal fields, spin-orbit coupling and hyperfine interaction, and can therefore be tuned to apply to other analogous transition metal defects or other SiC polytypes. For investigating their applicability in quantum information technology, the behavior of these defects was studied under the action of magnetic fields. This model's techniques give a good matching between theoretical and experimental findings with respect to anisotropy in the presence of a magnetic field, specifically with respect to the g-factor. The g-factor is a good qualitative and quantitative measure of how the localized spin states of the embedded defect respond to an external magnetic field, which is strongly related to the issue of qubit manipulation or operations. Although further analysis and tuning are needed to improve the quantitative match, qualitatively we are able to explain existent experimental observations for the V defect. Simultaneously, we create a basis for designing future experiments for the Mo defect, which will show whether microwave spin driving via a parallel or a perpendicular magnetic field is possible. We see from the model that this is possible if the states addressed have a zero orbital angular momentum component. These experiments will help us further tune the model for better fits, which in turn will give us a clear understanding of the fundamental physical phenomena at play. Our understanding of these phenomena is greatly aided by visualization using color maps, which proved to be a helpful tool in working with high-dimensional matrices.

7 Acknowledgements

I would like to thank my supervisor, Caspar van der Wal, and daily supervisor, Carmem Maia Gilardoni, for the opportunity and guidance in completing this project. Carmem has been of tremendous help along the way, and discussions with her were always eye-opening and motivating. In the peculiar circumstances of this year, Caspar, Carmem, Tom, Joop and Xu have created a supportive atmosphere from a distance.

References

[1] Montanaro, A. Quantum algorithms: an overview. *npj Quantum Inf* **2**, 15023 (2016). https://doi.org/10.1038/npjqi.2015.23

[2] Georgescu, I., Ashhab, S., Nori, F. Quantum simulation. *Rev. Mod. Phys.* **86**, 153 (2014). https://doi.org/10.1103/RevModPhys.86.153

[3] Buluta, I., Ashhab, S., Nori, F. Natural and artificial atoms for quantum computation. *Rep. Prog. Phys.* **74**, 104401 (2011). https://doi.org/10.1088/0034-4885/74/10/104401

[4] Bradley, C.E., Randall, J., Abobeih, M.H., Berrevoets, R.C., Degen, M.J., Bakker, M.A., Markham, M., Twitchen, D.J., Taminiau, T.H. A ten-qubit solid-state spin register with quantum memory up to one minute. *Phys. Rev. X* **9**, 031045 (2019). https://doi.org/10.1103/PhysRevX.9.031045

[5] Castelletto, S., Boretti, A. Silicon carbide color centers for quantum applications. *J. Phys. Photonics* **2**, 022001 (2020). https://doi.org/10.1088/2515-7647/ab77a2

[6] Cirac, J.I., Zoller, P., Kimble, H.J., Mabuchi, H. Quantum state transfer and entanglement distribution among distant nodes in a quantum network. *Phys. Rev. Lett.* **78**, 3221 (1997). https://doi.org/10.1103/PhysRevLett.78.3221

[7] Dreau, A., Tchebotareva, A., El Mahdaoui, A., Bonato, C., Hanson, R. Quantum frequency conversion of single photons from a nitrogen-vacancy center in diamond to telecommunication wavelengths. *Phys. Rev. Appl.* **9**, 064031 (2018). https://doi.org/10.1103/PhysRevApplied.9.064031

[8] Rueda, A., Hease, W., Barzanjeh, S., Fink, J.M. Electro-optic entanglement source for microwave to telecom quantum state transfer. *npj Quantum Inf* **5**, 108 (2019). https://doi.org/10.1038/s41534-019-0220-5

[9] Alkauskas, A., McCluskey, M.D., Van de Walle, C.G. Tutorial: Defects in semiconductors - Combining experiment and theory. *J. Appl. Phys.* **119**, 181101 (2016). https://doi.org/10.1063/1.4948245

[10] Doherty, M.W., Manson, N.B., Delaney, P., Jelezko, F., Wrachtrup, J., Hollenberg, L.C.L. The nitrogen-vacancy colour centre in diamond. *Phys. Rep.* **528**, 1-45 (2013). http://dx.doi.org/10.1016/j.physrep.2013.02.001

[11] Wrachtrup, J., Jelezko, F. Processing quantum information in diamond. *J.Phys.: Condens. Matter* **18**, S807S824 (2006). http://dx.doi.org/10.1088/0953-8984/18/21/S08

[12] Wolfowicz, G., Anderson, C.P., Diler, B., Poluektov, O.G., Heremans, F.J., Awschalom, D.D. Vanadium spin qubits as telecom quantum emitters in silicon carbide. *Sci. Adv.* **6**, eaaz1192 (2020). https://doi.org/10.1126/sciadv.aaz1192

[13] Bosma, T., Lof, G.J.J., Gilardoni, C.M. , Zwier, O.V., Hendriks, F., Magnusson, B., Ellison, A., Gallstrom, A., Ivanov, I.G., Son, N.T., Havenith, R.W.A., Van der Wal, C.H. Identification

and tunable optical coherent control of transition-metal spins in silicon carbide. *npj Quantum Inf* **4**, 48 (2018). https://doi.org/10.1038/s41534-018-0097-8

[14] Radulaski, M., Widmann, M., Niethammer, M., Zhang, J.L., Lee, S.Y., Rendler, T., Lagoudakis, K.G., Son, N.T., Janzen, E., Ohshima, T., Wrachtrup, J., Vuckovic, J. Scalable quantum photonics with single color centers in silicon carbide. *Nano Lett.* **17**, 17821786 (2017). http://dx.doi.org/10.1021/acs.nanolett.6b05102

[15] Falk, A.L., Buckley, B.B., Calusine, G., Koehl, W.F., Dobrovitski, V.V., Politi, A., Zorman, C.A., Feng, P.X.-L., Awschalom, D.D. Polytype control of spin qubits in silicon carbide. *Nat. Commun.* **4**, 1819 (2013). https://doi.org/10.1038/ncomms2854

[16] Son, N.T., Anderson, C.P., Bourassa, A., Widmann, M., Niethammer, M., Ul Hassan, J., Kaiser, F., Miao, K.C., Morioka, N., Babin, C., Ivanov, I.G., Wrachtrup, J., Awschalom, D.D. Developing silicon carbide for quantum spintronics. *Appl. Phys. Lett.* **116**, 190501 (2020). https://doi.org/10.1063/5.0004454

[17] Bourassa, A., Anderson, C.P., Miao, K.C., Onizhuk, M., Ma, H., Crook, A.L., Abe, H., Ul-Hassan, J., Ohshima, T., Son, N.T., Galli, G., Awschalom, D.D. Entanglement and control of single quantum memories in isotopically engineered silicon carbide. *arXiv:2005.07602*, (2020). https://arxiv.org/abs/2005.07602

[18] Seo, H., Falk, A., Klimov, P., Miao, K.C., Galli, G., Awschalom, D.D. Quantum decoherence dynamics of divacancy spins in silicon carbide. *Nat. Commun.* **7**, 12935 (2016). https://doi-org.proxy-ub.rug.nl/10.1038/ncomms12935

[19] Baur, J., Kunzer, M., Schneider, J. Transition metals in SiC polytypes, as studied by magnetic resonance techniques. *phys. stat. sol. (a)* **162**, 153-172 (1997). https://doi.org/10.1002/1521-396X(199707)162:1<153::AID-PSSA153>3.0.CO;2-3

[20] Hendriks, F., *Spin-active colour centres in silicon carbide, fundamental description and novel experimental techniques*, MSc thesis, Faculty of Science and Engineering, University of Groningen, Groningen, the Netherlands, 2018.

[21] Sakurai, J.J., Napolitano, J., *Modern Quantum Mechanics*, 2nd edition. USA: Pearson, 2010.

[22] Spindlberger, L., Csore, A., Thiering, G., Putz, S., Karhu, R., Ul Hassan, J., Son, N.T., Fromherz, T., Gali, A., Trupke, M. Optical properties of vanadium in 4H silicon carbide for quantum technology. *Phys. Rev. Appl.* **12**, 014015 (2019). https://doi.org/10.1103/PhysRevApplied.12.014015

[23] Ivady, V., Gallstrom, A., Son, N.T., Janzen, E., Gali, A. Asymmetric split-vacancy defects in SiC polytypes: A combined theoretical and electron spin resonance study. *Phys. Rev. Lett.* **107**, 195501 (2011). https://doi.org/10.1103/PhysRevLett.107.195501

[24] Tinkham, M., *Group theory and quantum mechanics*. Mineola, NY, USA: Dover, 1992.

[25] Ivady, V., Abrikosov, I.A., Gali, A. First principles calculation of spin-related quantities for point defect qubit research. *npj Comput Mater* **4**, 76 (2018). https://doi.org/10.1038/s41524-018-0132-5

A Parameters used to model the energy diagrams

The following parameters (values in meV) were used to model the energy diagrams of Hamiltonian H_0:

Table 4

E_{Od}	5
E_{Ot}	15
E_{C0}	-100
E_{C1}	50
E_{C2}	-1150
λ_{soc}	-3

B Clebsch-Gordan coefficients

From the theory of addition of angular momenta applied to the total angular momentum $\mathbf{J} = \mathbf{L}+\mathbf{S}$ (sum of orbital and spin angular momenta), one may expand an eigenstate of $\mathbf{J}$ in terms of eigenstates of $\mathbf{L}$ and $\mathbf{S}$:

$$|l\,s; j\,m_j\rangle = \sum_{m_l}\sum_{m_s}\langle l\,s; m_l\,m_s|l\,s; j\,m_j\rangle|l\,s; m_l\,m_s\rangle \tag{15}$$

where $\langle l\,s; m_l\,m_s|l\,s; j\,m_j\rangle$ are the Clebsch-Gordan coefficients.

For $l = 2$, $s = \frac{1}{2}$, the total angular momentum quantum number is $j = \frac{5}{2}$ (rightmost column) or $j = \frac{3}{2}$ (leftmost column), and the CG coefficients are:

Table 5

$CG_{j=3/2}$	$j = \frac{3}{2}, m_j$	m_l, m_s	$j = \frac{5}{2}, m_j$	$CG_{j=5/2}$
-	-	$2, \frac{1}{2}$	$\frac{5}{2}$	1
$\sqrt{\frac{4}{5}}$	$\frac{3}{2}$	$2, -\frac{1}{2}$	$\frac{3}{2}$	$\sqrt{\frac{1}{5}}$
$-\sqrt{\frac{1}{5}}$	$\frac{3}{2}$	$1, \frac{1}{2}$	$\frac{3}{2}$	$\sqrt{\frac{4}{5}}$
$\sqrt{\frac{3}{5}}$	$\frac{1}{2}$	$1, -\frac{1}{2}$	$\frac{1}{2}$	$\sqrt{\frac{2}{5}}$
$-\sqrt{\frac{2}{5}}$	$\frac{1}{2}$	$0, \frac{1}{2}$	$\frac{1}{2}$	$\sqrt{\frac{3}{5}}$
$\sqrt{\frac{2}{5}}$	$-\frac{1}{2}$	$0, -\frac{1}{2}$	$-\frac{1}{2}$	$\sqrt{\frac{3}{5}}$
$-\sqrt{\frac{3}{5}}$	$-\frac{1}{2}$	$-1, \frac{1}{2}$	$-\frac{1}{2}$	$\sqrt{\frac{2}{5}}$
$\sqrt{\frac{1}{5}}$	$-\frac{3}{2}$	$-1, -\frac{1}{2}$	$-\frac{3}{2}$	$\sqrt{\frac{4}{5}}$
$-\sqrt{\frac{4}{5}}$	$-\frac{3}{2}$	$-2, \frac{1}{2}$	$-\frac{3}{2}$	$\sqrt{\frac{1}{5}}$
-	-	$-2, -\frac{1}{2}$	$-\frac{5}{2}$	1

C The 11th root scale

When displaying values that differ greatly on the same plot, and we are mostly interested in signaling their presence rather than absolute values, we use a scale that resembles the logarithmic

scale. Specifically, we use the 11th root. We do this for ease of computation. In Fig. 14 we show the two functions which can be used interchangeably for illustration purposes.

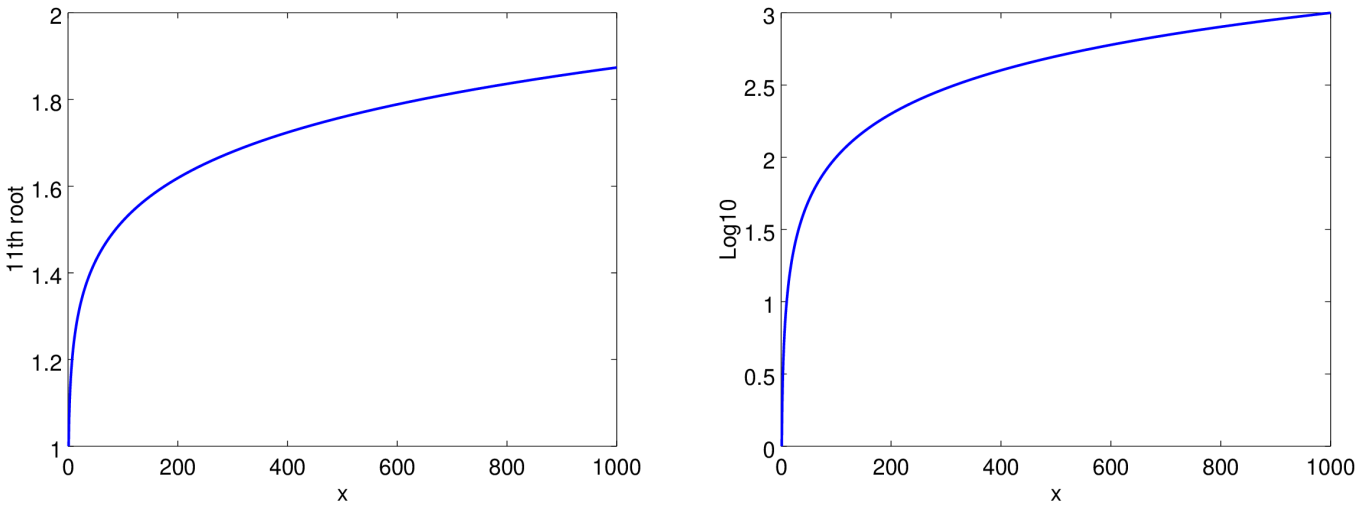

(a) (b)

Figure 14: Comparison of the 11th root- (left) and the log-function (right). The two functions' ranges differ slightly, but their shapes are very similar. For illustration purposes where the function value is not the most relevant, the two functions are interchangeable.

D Orbital angular momentum reduction parameter k

When starting to model the various interactions of the Mo^{5+} ion single valence electron in the 4d-orbitals, a first assumption one can make is that of pure d-orbitals. However, since the ion is not in a free state, but part of a crystal structure, its outer d-orbitals are not perfectly shielded from orbitals of surrounding atoms. This departure from pure d-orbitals is translated into an effective orbital g-factor, known as k. The k factor gives the amount by which the orbital g-factor g_l is reduced from its value of 1, so that k takes values between 0 and 1. Since this reduction affects the overall behavior of the electronic spin states under an applied magnetic field, measured in strength as the g-factor, we pay particular attention to how to deduce the k factor for our case here.

From the experimental measurement of T. Bosma et al. ([13]), it follows that the g-factor for a parallel magnetic field only ($\vec{B} \parallel \hat{z} \parallel \hat{c}$), $g_{\parallel}^{KD1} = 1.61$. This value is related to the observed splitting of energy states, and it is extracted using the effective spin Hamiltonian for the Zeeman interaction, which yields an energy splitting $\Delta E = \mu_B g_{\parallel} B_z$.

We know that on a microscopic scale, the energy splitting is described using the real spins Zeeman interaction Hamiltonian for a parallel field,

$$H_{Zee}^{z} = -\frac{\mu_B}{\hbar} B_z \cdot (g_e \vec{\mathbf{S}}_z + k\vec{\mathbf{L}}_z) - \frac{\mu_N}{\hbar} B_z \cdot g_p \vec{\mathbf{I}}_z \tag{16}$$

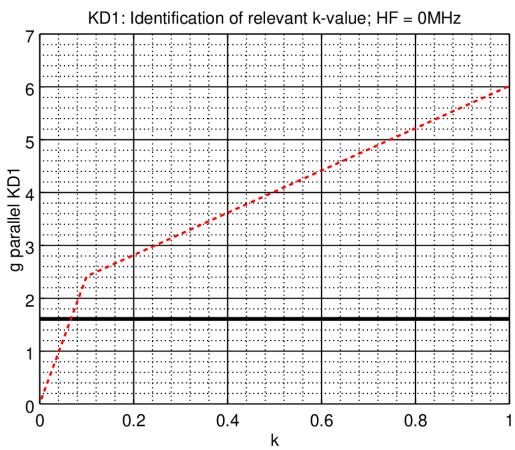

Figure 15: Plot of $g_{\|}$ versus k-factor for KD1. No hyperfine interaction is considered. Dotted line represents the calculated g-factor, while the solid line represents the value extracted from experiments by T. Bosma et al. [13]. The intersection of the two lines gives the k-value that most likely describes the reduction of orbital angular momentum for our system: $k \approx 0.065$.

By varying $k \in [0, 1]$, we calculate the eigenvalues of $H_0 + H_{hf} + H^z_{Zee}$ and use them to extract an equivalent effective $g_{\|}$ which we compare graphically with the experimentally extracted value. This is shown in Fig. 15.

E Effective Zeeman interaction Hamiltonian for a system with uniaxial symmetry

The effective Zeeman Hamiltonian in eq. 3 can be expanded as:

$$\tilde{H}_{zee} = -\frac{\mu_B}{\hbar} \begin{pmatrix} B_x & B_y & B_z \end{pmatrix} \begin{pmatrix} g_{xx} & g_{xy} & g_{xz} \\ g_{yx} & g_{yy} & g_{yz} \\ g_{zx} & g_{zy} & g_{zz} \end{pmatrix} \begin{pmatrix} \tilde{\mathbf{S}}_\mathbf{x} \\ \tilde{\mathbf{S}}_\mathbf{y} \\ \tilde{\mathbf{S}}_\mathbf{z} \end{pmatrix}$$

A system with uniaxial symmetry is defined by two sets of inequivalent directions: along the high-symmetry axis and perpendicular to it (defined as the basal plane). If we choose the z-axis of a Cartesian coordinate system as the high-symmetry axis, the effective g-tensor retains its diagonal terms only. Moreover, $g_{xx} = g_{yy} \neq g_{zz}$, and the effective Zeeman Hamiltonian can be rewritten as:

$$\tilde{H}_{zee} = -\frac{\mu_B}{\hbar} \begin{pmatrix} B_x & B_y & B_z \end{pmatrix} \begin{pmatrix} g_{xx} & 0 & 0 \\ 0 & g_{yy} & 0 \\ 0 & 0 & g_{zz} \end{pmatrix} \begin{pmatrix} \tilde{\mathbf{S}}_\mathbf{x} \\ \tilde{\mathbf{S}}_\mathbf{y} \\ \tilde{\mathbf{S}}_\mathbf{z} \end{pmatrix}$$

Below we show the matrix elements of the Zeeman interaction Hamiltonian for a field in the z-direction, and, separately, for a field in the x-direction for a fully symmetric system, and subse-

quently for a uniaxially symmetric system. For a fully symmetric system:

$$\langle H^z_{Zee}\rangle = \begin{pmatrix} -\frac{\mu_B B_z}{2} g_{zz} & -\frac{\mu_B B_z}{2}(g_{zx} - ig_{zy}) \\ -\frac{\mu_B B_z}{2}(g_{zx} + ig_{zy}) & \frac{\mu_B B_z}{2} g_{zz} \end{pmatrix}$$

$$\langle H^x_{Zee}\rangle = \begin{pmatrix} -\frac{\mu_B B_z}{2} g_{xz} & -\frac{\mu_B B_x}{2}(g_{xx} - ig_{xy}) \\ -\frac{\mu_B B_x}{2}(g_{xx} + ig_{xy}) & \frac{\mu_B B_z}{2} g_{xz} \end{pmatrix}$$

For a uniaxially symmetric system:

$$\langle H^z_{Zee}\rangle = \begin{pmatrix} -\frac{\mu_B B_z}{2} g_{zz} & 0 \\ 0 & \frac{\mu_B B_z}{2} g_{zz} \end{pmatrix}$$

$$\langle H^x_{Zee}\rangle = \begin{pmatrix} 0 & -\frac{\mu_B B_x}{2} g_{xx} \\ -\frac{\mu_B B_x}{2} g_{xx} & 0 \end{pmatrix}$$

F Hamiltonian of hyperfine interaction in cubic/spherical harmonics form

In operator form, the hyperfine interaction Hamiltonian considered here for the single electron in localized 4d-orbitals interacting with a spherically symmetric nucleus at a distance r away, is given by:

$$H_{hf} = \frac{\mu_0}{4\pi}\frac{g_e \mu_B g_p \mu_N}{\hbar^2}\frac{1}{r^3}\left(\vec{I}\cdot\vec{L} + 3\frac{(\vec{S}\cdot\vec{r})(\vec{I}\cdot\vec{r})}{r^2} - \vec{S}\cdot\vec{I}\right) \tag{17}$$

We consider the terms separately:

- The nucleus-electronic orbital angular momentum interaction:

$$\vec{I}\cdot\vec{L} = \frac{I_+L_- + I_-L_+}{2} + I_zL_z \tag{18}$$

- The dipole-dipole terms:

$$
\begin{aligned}
\vec{S}\cdot\vec{I} &= \frac{S_+I_- + S_-I_+}{2} + S_zI_z && (19)\\
(\vec{S}\cdot\vec{r})(\vec{I}\cdot\vec{r}) &= (S_xx + S_yy + S_zz)(I_xx + I_yy + I_zz) && (20)\\
&= S_xI_xx^2 + S_yI_yy^2 + S_zI_zz^2 + xy(S_xI_y + S_yI_x) + xz(S_xI_z + S_zI_x) + yz(S_yI_z + S_zI_y) && (21)\\
&= \left(\frac{S_+ + S_-}{2}\frac{I_+ + I_-}{2}\right)x^2 + \left(\frac{S_+ - S_-}{2i}\frac{I_+ - I_-}{2i}\right)y^2 + S_zI_zz^2 + && (22)\\
&+ xy\left(\frac{S_+ + S_-}{2}\frac{I_+ - I_-}{2i} + \frac{S_+ - S_-}{2i}\frac{I_+ + I_-}{2}\right) + && (23)\\
&+ xz\left(\frac{S_+ + S_-}{2}I_z + S_z\frac{I_+ + I_-}{2}\right) + && (24)\\
&+ yz\left(\frac{S_+ - S_-}{2i}I_z + S_z\frac{I_+ - I_-}{2i}\right) && (25)\\
&= xy\frac{1}{2i}(S_+I_+ - S_-I_-) + && (26)\\
&+ xz\frac{1}{2}(S_+I_z + S_-I_z + S_zI_+ + S_zI_-) + && (27)\\
&+ yz\frac{1}{2i}(S_+I_z - S_-I_z + S_zI_+ - S_zI_-) + && (28)\\
&+ (x^2 - y^2)\frac{1}{4}(S_+I_+ + S_-I_-) + && (29)\\
&+ \frac{1}{4}(S_+I_- + S_-I_+)(x^2 + y^2) + S_zI_zz^2 && (30)\\
&= d_{xy}\sqrt{\frac{4\pi}{15}}\frac{1}{2i}(S_+I_+ - S_-I_-)r^2 + && (31)\\
&+ d_{xz}\sqrt{\frac{4\pi}{15}}\frac{1}{2}(S_+I_z + S_-I_z + S_zI_+ + S_zI_-)r^2 + && (32)\\
&+ d_{yz}\sqrt{\frac{4\pi}{15}}\frac{1}{2i}(S_+I_z - S_-I_z + S_zI_+ - S_zI_-)r^2 + && (33)\\
&+ d_{x^2-y^2}\sqrt{\frac{4\pi}{15}}\frac{1}{2}(S_+I_+ + S_-I_-)r^2 + && (34)\\
&+ \frac{1}{4}(S_+I_- + S_-I_+)(x^2 + y^2) + S_zI_zz^2 && (35)\\
& && (36)
\end{aligned}
$$

$$
\begin{aligned}
3\frac{(\vec{S}\cdot\vec{r})(\vec{I}\cdot\vec{r})}{r^2} - \vec{S}\cdot\vec{I} &= d_{xy}\sqrt{\frac{4\pi}{15}}\frac{3}{2i}(S_+I_+ - S_-I_-) + && (37)\\
&+ d_{xz}\sqrt{\frac{4\pi}{15}}\frac{3}{2}(S_+I_z + S_-I_z + S_zI_+ + S_zI_-) + && (38)\\
&+ d_{yz}\sqrt{\frac{4\pi}{15}}\frac{3}{2i}(S_+I_z - S_-I_z + S_zI_+ - S_zI_-) + && (39)\\
&+ d_{x^2-y^2}\sqrt{\frac{4\pi}{15}}\frac{3}{2}(S_+I_+ + S_-I_-) + && (40)\\
&+ \frac{S_+I_- + S_-I_+}{4}\frac{3(x^2 + y^2)}{r^2} + S_zI_z\frac{3z^2}{r^2} - \frac{S_+I_- + S_-I_+}{2} - S_zI_z && (41)\\
& && (42)
\end{aligned}
$$

The last term Z^2:

$$
\begin{aligned}
Z^2 &= \frac{S_+I_- + S_-I_+}{4}\frac{3(x^2+y^2)}{r^2} + S_zI_z\frac{3z^2}{r^2} - \frac{S_+I_- + S_-I_+}{2} - S_zI_z && (43)\\
&= \frac{1}{r^2}\left(\frac{S_+I_- + S_-I_+)}{4}(3r^2 - 3z^2 - 2r^2) + S_zI_z(3z^2 - r^2)\right) && (44)\\
&= \frac{1}{r^2}\left(-\frac{S_+I_- + S_-I_+)}{4}(3z^2 - r^2) + S_zI_z(3z^2 - r^2)\right) && (45)\\
&= d_{z^2}\sqrt{\frac{4\pi}{15}}2\sqrt{3}\left(S_zI_z - \frac{S_+I_- + S_-I_+}{4}\right) && (46)
\end{aligned}
$$

Then, the hyperfine interaction Hamiltonian expressed using cubic harmonics is:

$$
\begin{aligned}
H_{hf} &= \frac{\mu_0}{4\pi}\frac{g_e\mu_B g_p\mu_N}{\hbar^2}\frac{1}{r^3}(\frac{I_+L_- + I_-L_+}{2} + I_zL_z + && (47)\\
&+ d_{xy}\sqrt{\frac{3\pi}{5}}i(S_-I_- - S_+I_+) + && (48)\\
&+ d_{xz}\sqrt{\frac{3\pi}{5}}(S_+I_z + S_-I_z + S_zI_+ + S_zI_-) + && (49)\\
&+ d_{yz}\sqrt{\frac{3\pi}{5}}i(-S_+I_z + S_-I_z - S_zI_+ + S_zI_-) + && (50)\\
&+ d_{x^2-y^2}\sqrt{\frac{3\pi}{5}}(S_+I_+ + S_-I_-) + && (51)\\
&+ d_{z^2}\sqrt{\frac{\pi}{5}}(4S_zI_z - S_+I_- - S_-I_+)) && (52)
\end{aligned}
$$

Given the transformation relations between cubic and spherical harmonics:

$$
\begin{aligned}
d_{z^2} &= Y_2^0 && (53)\\
d_{xz} &= \frac{Y_2^{-1} - Y_2^1}{\sqrt{2}}\\
d_{yz} &= i\frac{Y_2^{-1} + Y_2^1}{\sqrt{2}}\\
d_{xy} &= i\frac{Y_2^{-2} - Y_2^2}{\sqrt{2}}\\
d_{x^2-y^2} &= \frac{Y_2^{-2} + Y_2^2}{\sqrt{2}}
\end{aligned}
$$

the Hamiltonian H_{hf} can also be expressed using spherical harmonics ${Y_l}^m$:

$$
\begin{aligned}
H_{hf} &= \frac{\mu_0}{4\pi}\frac{g_e\mu_B g_p\mu_N}{\hbar^2}\frac{1}{r^3}(\frac{I_+L_- + I_-L_+}{2} + I_zL_z + && (54)\\
&+ Y_2^{-2}\sqrt{\frac{6\pi}{5}}S_+I_+ + && (55)\\
&+ Y_2^{-1}\sqrt{\frac{6\pi}{5}}(S_zI_+ + I_zS_+) + && (56)\\
&+ Y_2^{0}\sqrt{\frac{\pi}{5}}(4S_zI_z - S_+I_- - S_-I_+) + && (57)\\
&+ Y_2^{1}\sqrt{\frac{6\pi}{5}}(S_zI_- + I_zS_-) + && (58)\\
&+ Y_2^{2}\sqrt{\frac{6\pi}{5}}S_-I_-) && (59)
\end{aligned}
$$

Which, compactly may be written as:

$$
\begin{aligned}
H_{hf} &= (I_+ \quad I_- \quad I_z)\begin{pmatrix} 0 & \frac{\tau}{2} & 0 \\ \frac{\tau}{2} & 0 & 0 \\ 0 & 0 & \tau \end{pmatrix}\begin{pmatrix} L_+ \\ L_- \\ L_z \end{pmatrix} && (60)\\
&+ (S_+ \quad S_- \quad S_z)\begin{pmatrix} \tau Y_2^{-2}\sqrt{\frac{6\pi}{5}} & -\tau Y_2^{0}\sqrt{\frac{\pi}{5}} & \tau Y_2^{-1}\sqrt{\frac{6\pi}{5}} \\ -\tau Y_2^{0}\sqrt{\frac{\pi}{5}} & \tau Y_2^{2}\sqrt{\frac{6\pi}{5}} & \tau Y_2^{1}\sqrt{\frac{6\pi}{5}} \\ \tau Y_2^{-1}\sqrt{\frac{6\pi}{5}} & \tau Y_2^{1}\sqrt{\frac{6\pi}{5}} & 4\tau Y_2^{0}\sqrt{\frac{\pi}{5}} \end{pmatrix}\begin{pmatrix} I_+ \\ I_- \\ I_z \end{pmatrix} && (61)
\end{aligned}
$$

with $\tau = \frac{\mu_0}{4\pi}\frac{g_e\mu_B g_p\mu_N}{\hbar^2}\langle\frac{1}{r^3}\rangle$. When representing this Hamiltonian in a basis state set $|m_l\, m_s\, m_i\rangle$, we get terms like $\langle m_l|Y_2^{m_l}|m_l'\rangle$, which are the integral over a product of three spherical harmonics. The calculation of these integral is shown in appendix G.

G Integral over product of three spherical harmonics

The integration over the product of 3 spherical harmonics is given by:

$$
\begin{aligned}
I &= \int_0^{2\pi} d\phi \int_0^{\pi} \sin\theta d\theta Y_2^{m_1}(\theta,\phi)Y_2^{m_2}(\theta,\phi)Y_2^{m_3}(\theta,\phi) && (62)\\
&= \sqrt{\frac{(2\cdot 2+1)(2\cdot 2+1)(2\cdot 2+1)}{4\pi}}\begin{pmatrix} 2 & 2 & 2 \\ m_1 & m_2 & m_3 \end{pmatrix}\begin{pmatrix} 2 & 2 & 2 \\ 0 & 0 & 0 \end{pmatrix}
\end{aligned}
$$

where the Wigner 3j symbol $\begin{pmatrix} j_1 & j_2 & j \\ m_1 & m_2 & m \end{pmatrix}$ is related to the CG coefficients by:

$$
\begin{pmatrix} j_1 & j_2 & j \\ m_1 & m_2 & m \end{pmatrix} = (-1)^{j_1-j_2-m}\sqrt{\frac{1}{2j+1}}\langle j_1m_1, j_2m_2|j_1j_2, j, -m\rangle \qquad (63)
$$

The Wigner 3j symbol is symmetric with respect to cyclic permutations.

Then, the integral over a product of three spherical harmonics is non-zero if $\sum_i m_i = 0$.

H Composition of eigenstates of $\mathbf{H}_0$ and $\mathbf{H}_{hf}$

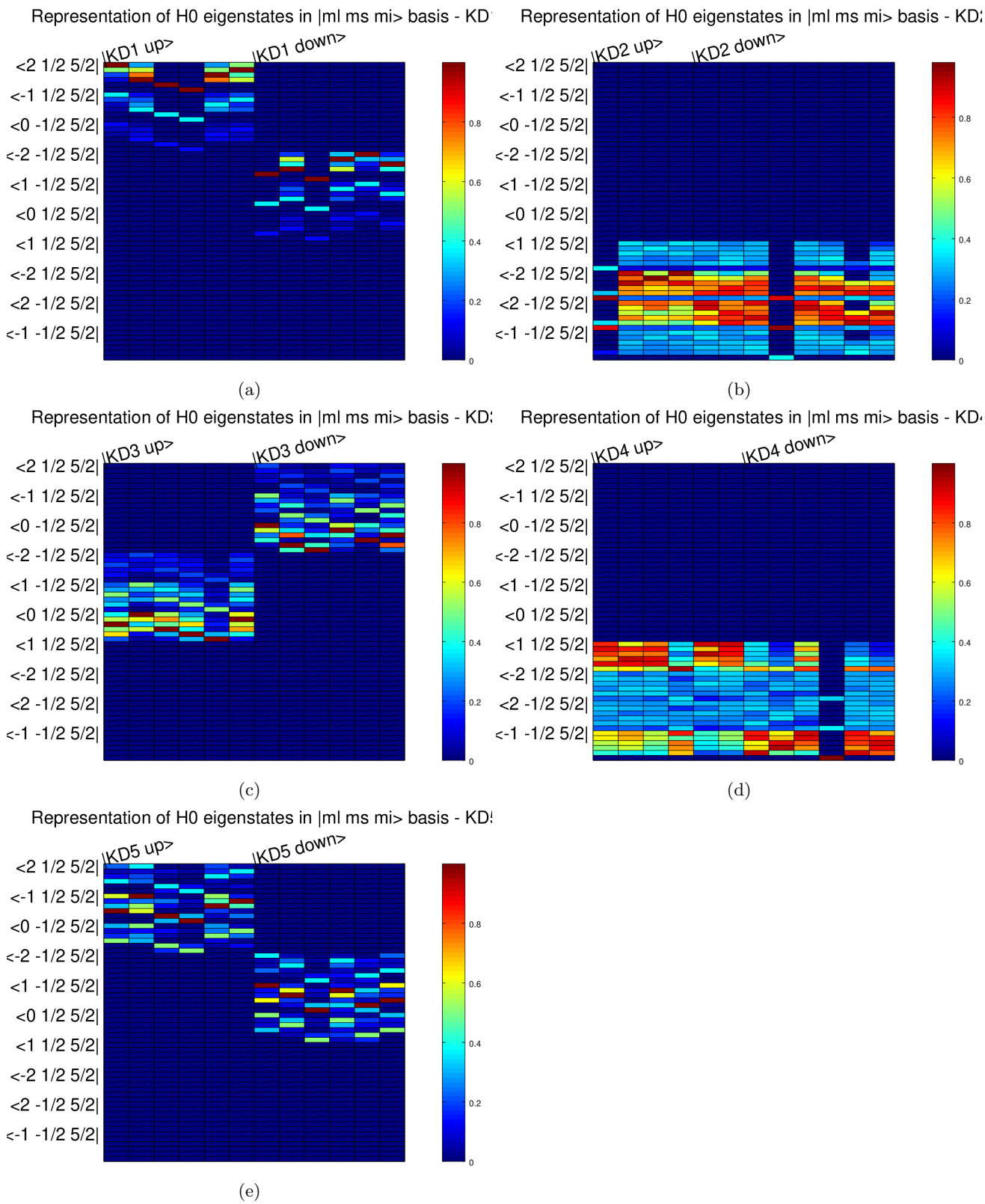

Figure 16: Composition of H_0 eigenstates in basis states $|m_l\, m_s\, m_i\rangle$, for KD1-KD5. The eigenstates are labeled by $|KD\uparrow,\downarrow\rangle$, depending on their behavior when an external magnetic field is applied (along the crystal c-axis). A log-like scale is used, in order to capture all non-zero probability coefficients (see appendix C). Within a figure, the columns represent eigenstates, and the rows represent basis states.

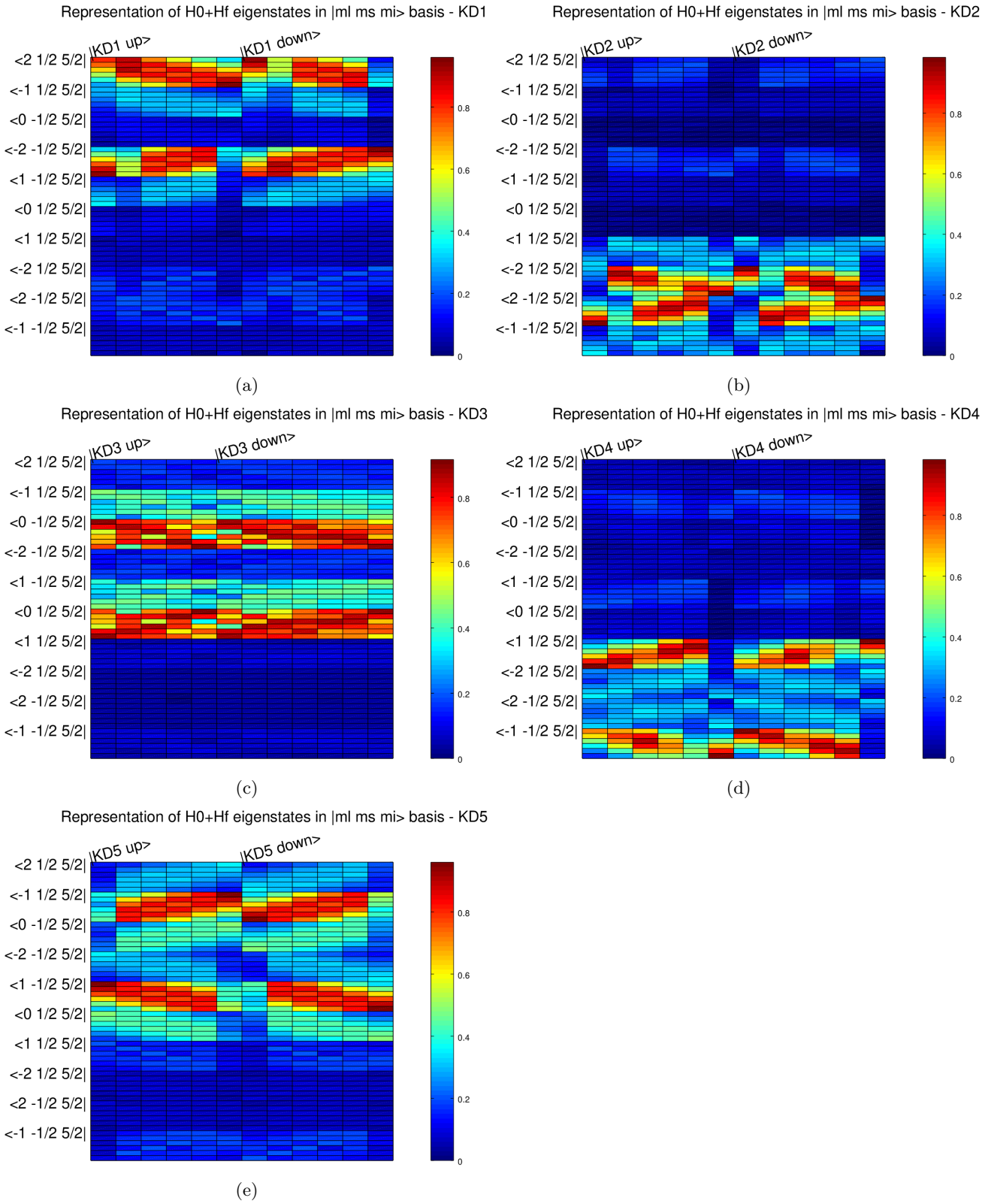

Figure 17: Composition of $H_0 + H_{hf}$ eigenstates in basis states $|m_l\, m_s\, m_i\rangle$, for KD1-KD5. The eigenstates are labeled by $|KD\uparrow,\downarrow\rangle$, depending on their behavior when an external magnetic field is applied (along the crystal c-axis). A log-like scale is used, in order to capture all non-zero probability coefficients (see appendix C). Within a figure, the columns represent eigenstates, and the rows represent basis states.